ELSEVIER

Contents lists available at ScienceDirect

Additive Manufacturing

journal homepage: www.elsevier.com/locate/addma





Simulation of fiber-induced melt pressure fluctuations within large scale polymer composite deposition beads

Aigbe Awenlimobor^a, Douglas E. Smith^{a,*}, Zhaogui Wang^b

- ^a Department of Mechanical Engineering, School of Engineering and Computer Science, Baylor University, Waco, TX 76798, USA
- ^b Department of Mechanical Engineering, Naval Architecture and Ocean Engineering College, Dalian Maritime University, Dalian 116000, China

ARTICLE INFO

Keywords: Large area additive manufacturing (LAAM) Microstructures Porosity Computational Modelling Finite element analysis (FEA)

ABSTRACT

The process-structure-property relationship in Large Area Additive Manufacturing (LAAM) technology is an ongoing area of research as the inherent microstructural properties (chiefly fibers and voids) affect the performance of printed parts. Unfortunately, we currently lack adequate understanding of micro void nucleation and evolution during the LAAM and fused deposition modelling (FDM) processes. Modeling of the polymer melt flow during the extrusion process is important in understanding the underlying microstructural formation and associated properties of the print, that determines the part performance in service conditions. In this paper we compute fiber-induced local pressure fluctuations which may promote void formation in the bead's microstructure. On a macro-scale, we determine flow fields of a purely viscous, Newtonian planar polymer deposition flow through a LAAM nozzle which are utilized on a micro-scale model where we simulate the evolution of a single ellipsoidal fiber along streamlines obtained from the macro-model. On the micro-scale, we determine instantaneous values of the translational and rotational velocities of the rigid ellipsoidal fiber that satisfies a balance of hydrodynamic forces and couples on the fiber's surface based on a Newton Raphson algorithm and we track the fiber's motion along the flow path via an explicit numerical iterative algorithm. Model verification is achieved by benchmarking results with solutions from well-known Jeffery's equation of motion of a particle in homogeneous simple shear flow. We account for rotary diffusivity due to short-range fiber-fiber interaction in the FEA simulation by determining an effective fluid domain size representative of the interaction coefficient of the melt flow through a correlation analysis that yields an equivalent steady state orientation based on the Advani-Tucker equation. We also consider different possible motions of the fiber along individual LAAM flow paths from a given set of random initial fiber conditions to determine pressure bounds on the fiber surface along each streamline. For improved computational efficiency, calculations are carried out with respect to the fiber's local coordinate axes to overcome the rigor of adaptive remeshing during the quasi-transient analysis. Results show low pressure extremes near the fiber's surface which varies across the printed bead as well as through its thickness. Discussion is provided to gain insight into the effect of low-pressure extremes on micro void formation, particularly at the nozzle exit and during die swell/expansion.

1. Introduction

Polymer composite extrusion-deposition, which include small-scale Fused Filament Fabrication (FFF) and large-scale Large Area Additive Manufacturing (LAAM), has gained widespread attention among other Additive Manufacturing (AM) technology because of its comparatively high production speed and low production cost with extensive design flexibility and material selection [1]. Knowledge of the microstructure development during FFF and LAAM processing can be used to improve the quality and performance of the composite parts produced by these

AM technologies. While the addition of short carbon fibers in the polymer feed stock yields improved thermo-mechanical properties in the printed part, fiber inclusions have also been shown to create micro-voids within the microstructure of a printed bead that results in lower-than-expected part quality and impaired part performance in service [2–5]. Further, micro-voids within the LAAM bead microstructure have been shown to appear when fibers are present but do not occur when neat polymers are used to produce beads under the same operating conditions [5]. Vaxman et al. [6] identified micro-void nucleation mechanisms in fiber-filled polymers, and micro-voids are more

E-mail address: douglas_e_smith@baylor.edu (D.E. Smith).

^{*} Corresponding author.

prevalent in higher fiber content composites [7]. Unfortunately, micro-voids in LAAM polymer composite beads degrade their structural integrity, but the influence of suspended fibers on micro-void formation during the processing of LAAM beads is not well understood. This paper considers mechanisms that promote intralayer micro-void nucleation within polymer composite beads during the extrusion-deposition additive manufacturing process.

Voids within polymer extrusion-deposition parts primarily appear in two forms: 1) interlayer voids that occur between beads, and 2) intralayer micro-voids that form within the microstructure of a bead during processing. Most interlayer voids are prismatic shaped and can be controlled somewhat with lateral bead space and post-deposition compaction (i.e., with a tamper or roller). Of the two types of voids, interlayer voids aligned in the loading direction are less detrimental to the mechanical properties of the AM printed composite than intralayer micro-voids within the bead microstructure (denoted as micro-voids in this paper) [5]. Alternatively, intralayer micro-voids serve as sites of stress concentration that reduce the load bearing capacity of the polymer composite material.

Knowledge of the micro-void morphology within a composite can provide useful insight into the originating source and type of micro-voids [8]. For example, randomly dispersed ellipsoidal shaped micro-voids that form at the fiber-matrix interface likely result from compromised integrity of the sizing agent [8]. Alternatively, spherical shaped micro-voids isolated within the matrix may result from several process related mechanisms. Indeed, micro-void development within an extrusion-deposition AM bead has been shown to depend on the polymer melt material, operating conditions, in addition to other external factors [6,9]. Encapsulation of low molecular weight substances within the raw pellets during the compounding process is a known source of micro-void formation within beads which can be reduced by adequate venting measures [6,10].

A significantly important mechanism of micro-void development within the polymer melt is that of bubble nucleation and growth [6] where micro-void development is dependent on the local fluid pressure of the polymer melt [11-14,16,17]. For example, in the moisture/volatile absorption-desorption induced void formation mechanism [11,12,14] which is based on classical nucleation theory, a requirement for void nucleation is the occurrence of sufficiently low localized fluid pressure below the vapor pressure of the gaseous phase of the dissolved volatile contents. Detailed description of this mechanism has been provided in Appendix I. Alternatively, in the theoretical development of the restrained volume contraction nucleation mechanism which occurs due to thermal stratification and non-uniform cooling across the extrudate during solidification, void nucleation can occur at locations within the flow where the local fluid pressure drops below the atmospheric pressure [16-18]. Studies have shown that faster cooling rate during extrudate solidification resulted in higher levels of micro-void contents within the polymer composite [6,10]. Yang et al. [19] studied the distribution of the micro-void content across regions of the melt in a FFF extruder and the deposited extrudate. Yang found insignificant void content in the polymer melt within the filament feed and heating/extrusion zones of the extruder and nozzle. Alternatively, he showed that the micro-void content increased significantly near the nozzle exit which then decreased upon deposition of the bead on the moving bed. The two-phase nature of polymer melt fiber suspension suggests that the dominant mode of micro-void formation is heterogenous [5,13,15]. The mismatch in the coefficient of thermal expansion between the reinforcing fiber agent and the matrix have been shown to promote micro-void formation at the fiber-matrix interface during cooling [19]. Vaxman et al. [6] showed that suspended fibers influence micro-void nucleation and that micro-voids preferentially form at the ends of fibers. He further showed that micro-void concentration depends on the fiber's aspect ratio, the rheological properties of the suspension and extrusion-deposition operating conditions.

More recently, computational techniques including the finite-

difference method (FDM), finite-volume method (FVM), finite element method (FEM), smoothed particle hydrodynamics (SPH), and discrete element method (DEM) etc. have been used to better understand the extrusion-deposition process in an effort to characterize the polymer melt flow behavior and obtain process parameters and field states. Xia et al. [20] developed a FVM approach to simulate the polymer melt flow and subsequent cooling in the FDM process. Heller et al. [21], Wang et al. [22-24] and Russell et al. [25] used FEM to simulate the flow of fiber filled polymer melt in a LAAM extruder nozzle to evaluate the orientation state of suspended short carbon fibers and the resulting thermo-mechanical properties. Phan et al. [26] used region dependent modelling of the FFF process to understand the melting and pressurization mechanisms involved. He combined a generalized Newtonian fluid (GNF) model in the heated region of the extruder with a viscoelastic model for the nozzle region and showed that a significant pressure drop occurs across the capillary section of the nozzle. Shadvar et al. [27] used FEM to study the polymer melt behavior of ABS in the extruder and die swell of the extrudate and compared flow fields from the simulation with that obtained from experiments. This work showed that the pressure-drop across the nozzle varied directly and inversely with the temperature and flow rate of the extruded filament, respectively. Yang et al. [28] used a coupled SPH and DEM particle method to simulate the FFF process of carbon fiber reinforced polymers where the focus was on fibers orientation and deformation. Ouyang et al. [29] employed a coupled microstructure constitutive fiber model with SPH considering temperature dependence to predict fiber orientation and resulting thermo-mechanical properties.

Among pioneering efforts that simulate the motion of a single ellipsoidal rigid particle suspended in a viscous fluid are works such as model by Oberbeck [30] and Edwardes [31], where Jeffery's model [32] served as the basis for their notable work. Various extensions to Jeffery's model with added complexity have evolved over time to predict the motion of suspended particles which considered various factors not included in Jeffery's model assumption. For example, Hinch et al. [33] showed that particles which do not conform to the axisymmetric shape of ellipsoidal solid suspended in simple shear viscous flow exhibit significant deviation of its motion from Jeffery's orbit. Zhang et al. [34] used a coupled FEM - Brownian dynamic simulation (BDS) approach to study the added effect of Brownian disturbance from surrounding fluid molecules on the fiber's motion via a Langevin approach and found its contribution to be dependent on the Peclet number. Férec et al. [35] studied the effect of shear-thinning on suspended particle motion in simple shear flow of a dilute suspension with non-Newtonian rheological properties based on a two-dimensional (2D) FEM analysis and showed insignificant deviation from Jeffery's orbit. A three-dimensional (3D) analysis by Abhati et al. [36] based on an asymptotic solution showed significant deviation from the Jeffery's tumbling period while identifying a sensitivity to initial conditions. The effect of a fiber's flexural properties and its back-coupling with interacting fluid has also been investigated by various researchers. Most models for this purpose employ a particle-based discretization technique using bead or rod chains interlinked with joints having directional stiffness and failure property definition to investigate the complex dynamics of the suspended particle in viscous flow field. Examples of such models include work by Skjetne et al. [37], Yamamoto et al. [38], and Yamanoi et al. [39] which are included in the overview of existing element-based simulations for fiber reinforced polymers by Kugler et al. [40]. The primary focus of these earlier works has been on fiber motion with little attention being given to the pressure field on and/or near the surface of a suspended fiber.

Fiber suspension analysis, particularly that performed for polymer composite melt extrusion-deposition processes, has almost exclusively focused on fiber orientation and spatial distribution within the microstructure. However, little attention has been given to micro-void formation and evolution during extrusion-deposition or to understand how the suspended fibers influence micro-void development. The main

objective of this article is to present a computational approach aimed at understanding mechanisms that may promote moisture/volatile induced micro-void nucleation on or near suspended fibers within the bead microstructure produced by polymer extrusion-deposition process via a multiscale modelling methodology. While our approach would be applicable to both filament based FFF and LAAM systems and other extrusion-based processes, our focus here is on the large scale polymer composite deposition. In the macroscale model, we develop a twodimensional (2D) planar flow model for predicting melt flow velocity and fiber orientation within the polymer melt during the extrusiondeposition process in a LAAM extruder nozzle. Then a micro-scale model is developed following the approach in Zhang et al. [41-43] which is based on Jeffrey's model assumptions for suspended particles [30]. We simulate the evolution of a single ellipsoidal fiber along streamlines of the polymer melt flow through the nozzle and onto the print platform utilizing the field responses (velocity, velocity gradients and pressure) obtained from the macroscale model which define boundary conditions in the micro-model. Then, a single fiber's translational and rotational velocities are computed by zeroing the net hydrodynamic forces and torques on the fiber's surface where its orientation and evolution along the flow path are updated based on an explicit iterative numerical algorithm which incorporates velocities and pressures from the macro-model. The micro-model is validated by comparing results of fiber motion and pressure distribution on the fiber surface with Jeffery's analytical model equations [30] for the motion of a single particle suspended in purely viscous shear flow. We account for rotary diffusivity due to short-range fiber-fiber interaction in the micro-model FEA simulation by determining an effective fluid domain size that mitigates Jeffery's rotation to match that predicted by the Advani-Tucker fiber orientation evolution equation. We also consider the fiber's evolution along various flow paths based on a given set of random initial fiber conditions to determine pressure bounds on the fiber surface across the melt flow.

The pressure distribution on the fiber's surface as it travels along streamlines through the LAAM nozzle and onto the print bed, particularly within the regions of die swell at the nozzle exit, provides insight into a potential mechanism that could promote micro-void formation within printed beads. Knowledge of the relationship between process operating parameters and void formation and evolution can be used to control the quality of printed parts [6,9].

2. Methodology

A multiscale modelling approach is developed in this work to better understand micro-void initiation within the beads printed with the LAAM extrusion-deposition process. The computational method here includes a macro-scale model which is used to calculate velocities and pressure along streamlines from the polymer melt flow solution in the extrusion-deposition process, and a micro-scale model which simulates the motion of a single rigid ellipsoidal particle based on the fluid flow solution along the macro-model streamlines. Our approach is a one-way coupling where computed velocities and pressures calculated along macro-model streamlines serve as inputs to define boundary conditions in the micro-model. A Newtonian fluid is assumed in both models. The material properties of the polymer melt employed in this study are taken from Heller et al. [21] and Wang et al. [23] which include a density of $1154kgm^{-3}$ and kinematic viscosity of $817Pa \bullet s$ (i.e., 13% by weight carbon fiber filled ABS at 230 °C with a shear rate of 100 s^{-1}). In all of the discussion to follow, a 'fiber' is a rigid two-dimensional ellipsoidal solid having an aspect ratio of $r_e = a/b$ where a and b are the lengths of the major and minor ellipsoidal axes.

2.1. Macro-model - 2D planar extrusion-deposition flow

A typical extrusion-deposition process of fiber filled polymer through

a LAAM extrusion nozzle and the subsequent single bead deposition on a translating substrate is shown in Fig. 1a. The internal nozzle geometry used in this study is based on the Strangpresse (Strangpresse, LLC, Youngstown, Ohio, USA) Model 19 LAAM single screw extruder nozzle where an annotated schematic representation of its internal nozzle geometry appears in Fig. 1b. The 2D planar flow domain consists of the internal nozzle geometry region and a single bead layer deposited on the substrate that translates laterally with respect to the nozzle. (cf. Fig. 2a). The FEM formulation is briefly described here where additional modelling details of planar deposition flow can be found in Zhang, et al. [44].

The governing equations for polymer melt flow within the nozzle and the printed bead are defined by Stokes's equation based on the assumptions of no inertia in the fluid, the polymer melt is a creeping flow with a low Reynolds number (i.e., Re<<1), and the polymer melt is an isothermal, incompressible, Newtonian fluid. Based on these assumptions, the mass and momentum conservation equations reduce to [44].

$$\underline{\nabla} \bullet \underline{v} = 0 \tag{1}$$

$$\underline{\nabla} \bullet \underline{\sigma} + f = 0 \tag{2}$$

where ∇ is the gradient operator in 2D, \underline{v} is the fluid velocity vector, \underline{f} is the body force vector, and $\underline{\sigma}$ is the Cauchy stress tensor given as:

$$\underline{\sigma} = \underline{\tau} - p\underline{I} \tag{3}$$

In the above, p is the fluid hydrostatic pressure, $\underline{\underline{I}}$ is the identity tensor and $\underline{\underline{\tau}}$ is the deviatoric stress tensor which is written for a Newtonian fluid as:

$$\underline{\tau} = 2\mu\underline{\Gamma} \tag{4}$$

where μ is the Newtonian viscosity and $\underline{\underline{\Gamma}}$ is the second-order rate of deformation tensor. Note that Eq. (4) does not include the influence of fiber orientation on the deviatoric stress.

The ANSYS Polyflow (Ansys, Canonsburg, PA, USA) commercial software is used for the macro-model polymer melt flow extrusion-deposition analysis. Fig. 2a illustrates the quasi-steady fluid domain and boundary conditions for the 2D polymer melt flow model. Using data from Heller et al. [21] and Wang et al. [23,43], the average normal velocity of 24 mm/s is prescribed at the nozzle inlet Γ_1 , and the velocity of the moving substrate and deposited material is 101.6 mm/s in the positive x-direction which is imposed on Γ_4 and Γ_5 . A no slip boundary condition is imposed on the nozzle inner wall Γ_2 and a free-surface boundary condition is prescribed on the exposed surface Γ_3 of the deposited material. Fig. 2b shows computed velocity streamlines that form between the nozzle inlet Γ_1 and the bead flow exit Γ_5 . Also shown in Fig. 2b are feature streamlines 4, 10, and 18 in addition to zones of interest 1, 2, and 3 to be discussed below.

The velocity magnitude $|\underline{\nu}|$ and scalar magnitude of deformation tensor $\dot{\gamma}=\sqrt{2\underline{\Gamma}}$: $\underline{\Gamma}$ appear in Figs. 3a, and 3b, respectively. Computed velocities in Fig. 3a show an increase in velocity magnitude from the edge of the nozzle to its center as expected. It follows that material along streamlines near the edges of the nozzle have a higher extrusion-deposition time compared to those closer to the center. The velocity contours (see for example, Figs. 5 and 6 in Ref. [44]) show a parabolic velocity distribution across transverse sections of extruder nozzle except near the entrance and exit of the straight capillary portion of the nozzle. Melt flow in these transition regions is characterized by sharp transitions of velocity and velocity gradients along the inside wall of the extrusion nozzle. Upon deposition onto the print bed, the melt flow attains a uniform velocity throughout the bead material where all stresses reduce to zero.

The plot of velocity gradient in Fig. 4 shows unusually high values occurring at the sharp corners of the flow field due to singularities in the velocity solution where the polymer melt flow transitions from a no-slip



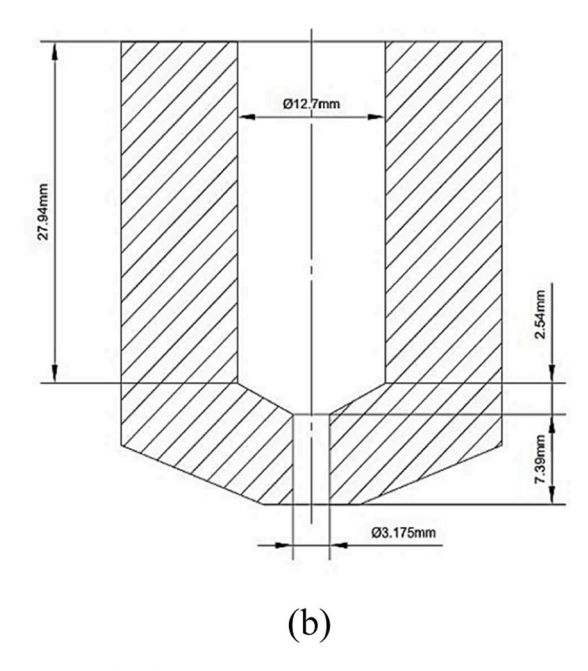


Fig. 1. a) Polymer deposition process, b) Extrusion die schematic. [21,22,44].

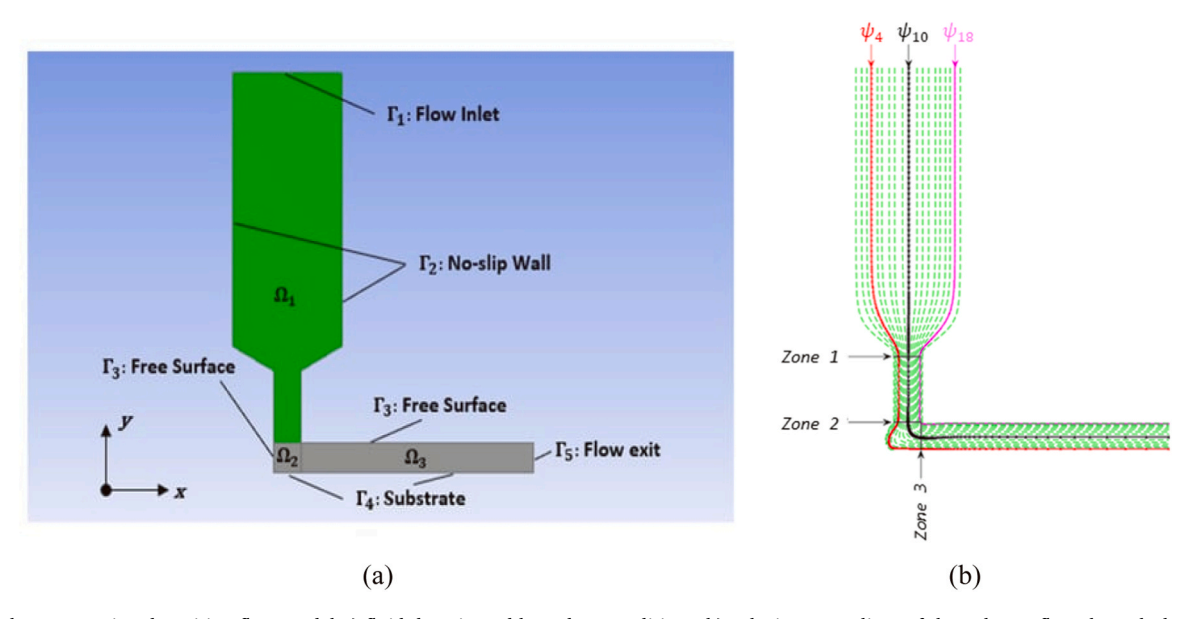


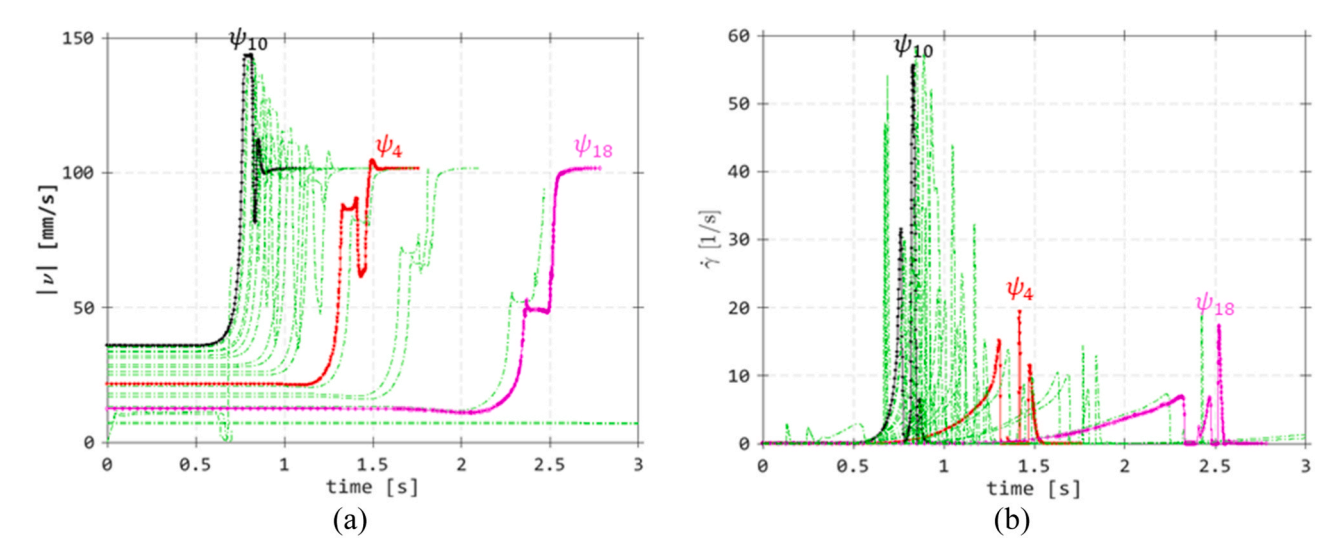
Fig. 2. 2D Planar extrusion-deposition flow model a) fluid domain and boundary conditions, b) velocity streamlines of the polymer flow through the nozzle with feature streamlines highlighted.

to a free surface boundary condition, which we attribute a posteriori to be responsible for unexpected behavior of the fiber's motion along streamlines close to these locations. In this figure, as well as in all of the micro-model results, ν_x and ν_y are the components of the velocity vector $\underline{\nu}$ in the x- and y-directions, respectively. We see from Fig. 4 that the velocity gradient component - $\partial \nu_y/\partial x$ dominates near the nozzle exit and is seen to increase in magnitude when moving outward from the center streamline towards those near the edge of the nozzle.

2.2. Micro-model - 2D single fiber motion

Simulation of a rigid ellipsoidal fiber motion along streamlines of the polymeric melt flow is performed in this work using a custom FEM code developed in MATLAB (MathWorks, Natick, MA, USA). The single fiber micromodel is governed by Stokes's assumption of negligible inertia and

negligible thermal effects and includes an isotropic homogenous Newtonian fluid that is the same as that used in the extrusion-deposition macro-model described above. Our algorithm for the micro-model simulation of a single 2D rigid ellipsoidal particle is derived from the work in Zhang et al. [41–43]. The flow domain for the 2D single fiber micro-model appears in Fig. 5a where we assume no slip occurs on the fiber surface and there is no flux across the fiber surface. Velocity, velocity gradient and pressure computed along streamlines of the extrusion-deposition macro-model described above are used to prescribe boundary conditions on the micro-model flow boundaries as a function of time. To impose these values in the micro-model, three essential boundary conditions are prescribed with respect to the fiber's local coordinate axes (cf. Fig. 5b). FEM solutions are obtained by applying the essential boundary conditions to a fixed mesh which is rotated with the local fiber axes. Rotating the model in this manner significantly reduces



 $\textbf{Fig. 3. a) Velocity magnitude} \ |\underline{\textbf{\textit{v}}}| \ \textbf{\textit{b}) scalar magnitude of second order deformation tensor for various streamlines with feature streamlines highlighted.} \\ ^{11}$

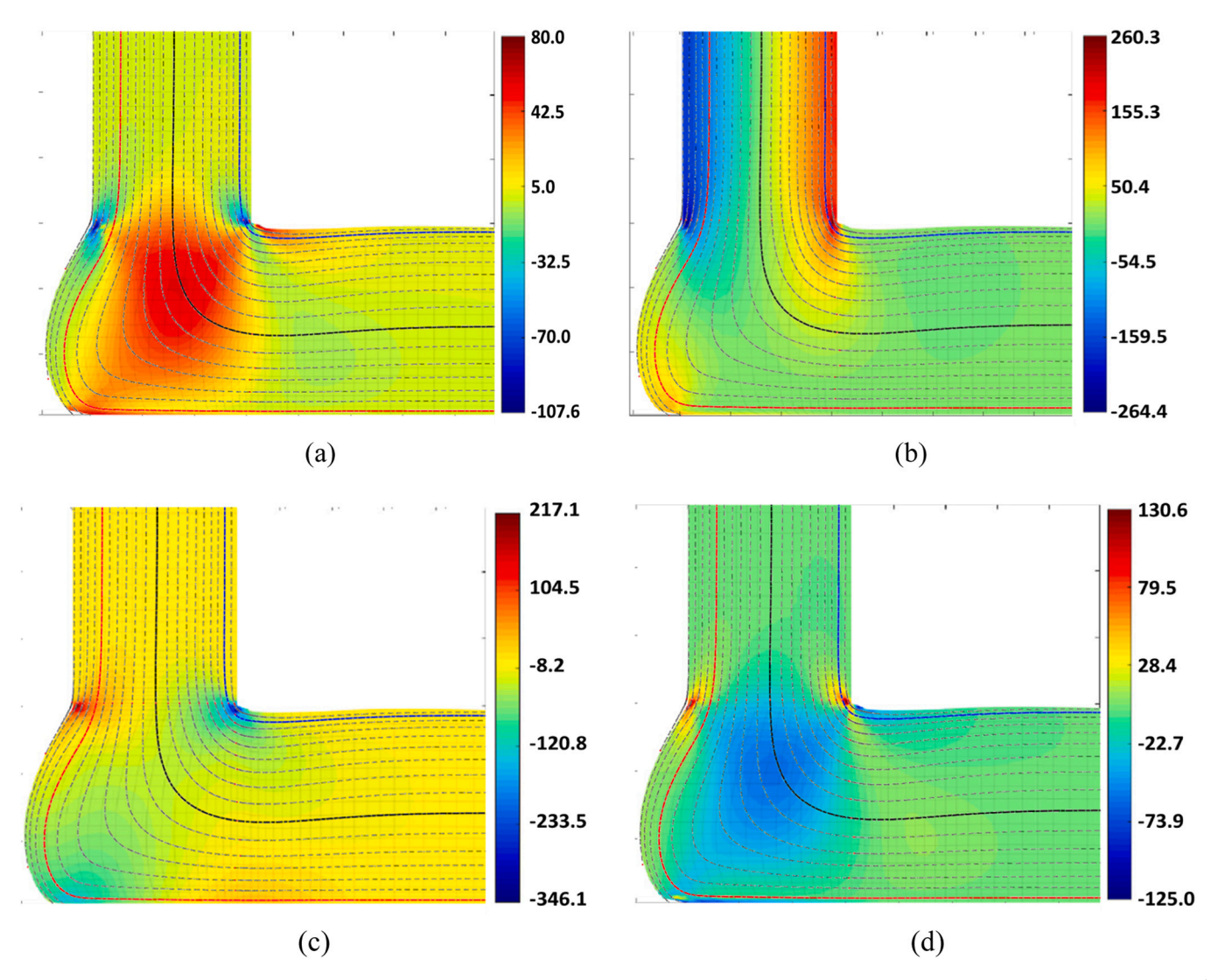


Fig. 4. Velocity gradient contours near extrusion-deposition transition zones (a) $\partial v_x/\partial x$, (b) $\partial v_y/\partial x$, (c) $\partial v_x/\partial y$, (d) $\partial v_y/\partial y$. The units of the velocity gradients are s^{-1} .

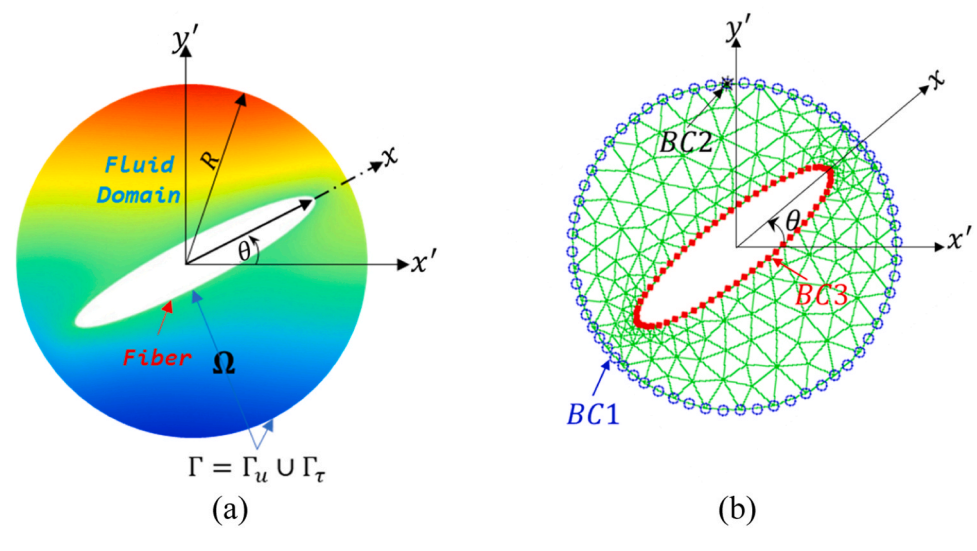


Fig. 5. Micro-model showing a) flow domain b) prescribed boundary conditions [41].

computation time by maintaining a constant FEA system matrix, avoiding the need of remeshing the domain and/or recalculating the system matrix and its decomposed form at each iteration time step.

The far-field velocities on the fluid domain boundary $\underline{u}^{\text{BC1}}$ of the micro-model are defined from the streamline velocities and velocity gradients obtained from the macro-model velocity solution at each time t of the single fiber evolution solution. Referring to Fig. 5b, the prescribed velocities $\underline{u}^{\text{BC1}}$ is defined in terms of the 2D transformation matrix \underline{T}_a as:

$$\underline{u}^{\text{BC1}} = \underline{\underline{T}}_{\theta}^{T} \underline{u}_{\psi} + \underline{\underline{T}}_{\theta}^{T} \underline{\nabla} \underline{u}_{\psi} \underline{\underline{T}}_{\theta} \underline{T}^{\text{BC1}}$$

$$(5)$$

where the velocity \underline{u}_{ψ} for streamline ψ , the 2D gradient operator $\underline{\nabla}$, and the position vector \underline{r} are, respectively,

$$\underline{u}_{\underline{\psi}} = \begin{bmatrix} u_x \\ u_y \end{bmatrix}_{\underline{\psi}}, \ \underline{\nabla}_{\underline{v}}^T = \begin{bmatrix} \partial/\partial x & \partial/\partial y \end{bmatrix}, \ \underline{r} = \begin{bmatrix} x \\ y \end{bmatrix}$$

In the above, the transformation matrix $\underline{\underline{T}}_{\theta}$ is defined in terms of the in-plane fiber orientation angle θ is given as:

$$\underline{\underline{T}}_{\theta} = \begin{bmatrix} \cos\theta & \sin\theta \\ -\sin\theta & \cos\theta \end{bmatrix} \tag{6}$$

A single prescribed pressure p_{BC2} is defined according to Eq. 7 on a far-field node BC2 located on the fluid domain surface where its value is computed from the macro-model streamline pressure p_{ψ} as:

$$p_{BC2} = p_{\psi} \tag{7}$$

The prescribed velocities $\underline{u}^{\text{BC3}}$ on the fiber's surface are transformed according to the equation of rigid body motion which is defined based on the translational velocity \underline{u}_{c} and rotational velocity $\hat{\theta}$ of the fiber's center as:

$$\underline{u}^{\text{BC3}} = \underline{\underline{T}}_{q}^{T} \underline{u}_{c} + \widehat{\dot{\theta}} \times \underline{r}^{\text{BC3}}$$
(8)

Discretization of the micro-model fluid domain is achieved using a radial seed of 60-unit cells with a unidirectional geometric bias of 1.1 and circumferential seed of 60-unit cells resulting in a total of 1800 triangular elements as shown in Fig. 6a. We employ a 6-node quadratic,

iso-parametric triangle serendipity element (cf. Fig. 6b) which has been found to give accurate results for low Reynolds number fluid flow problems [45].

The element system matrices and force vectors are derived from a mixed method representation of the Galerkin formulation [46] as:

$$\int_{c_e} \underline{\phi}^{eT} \underline{B}^e d\Omega^e \underline{u}^e = 0 \tag{9}$$

$$\int_{\Omega^{e}} \underline{\underline{B}}_{s}^{eT} \mu \underline{\underline{C}}_{o} \underline{\underline{B}}_{s}^{e} d\Omega^{e} \underline{\underline{u}}^{e} - \int_{\Omega^{e}} \underline{\underline{B}}^{eT} \underline{\phi}^{e} d\Omega^{e} \underline{\underline{p}}^{e} - \int_{\Omega^{e}} \rho \underline{\underline{N}}^{eT} \underline{\underline{f}} d\Omega^{e} - \int_{\Gamma_{\tau}^{e}} \underline{\underline{N}}_{e}^{eT} \underline{\underline{i}} d\Gamma^{e} = 0$$
(10)

where.

 $\underline{\phi}^e$ & $\underline{\underline{N}}^e$ are the pressure and velocity interpolation function matrices, respectively,

 \underline{B}^e & B_s^e are strain-displacement matrices, respectively,

 $\underline{u}^e \& \underline{p}^e$ are, respectively, the velocity and pressure degrees-of-freedom (dof) at the respective element nodes,

 Γ^e & Ω^e are the element boundary surfaces and domain of integration, respectively, and.

 \underline{f} and $\underline{\bar{t}}$ are the body force and surface traction vectors, respectively. The mixed method in Eqs. (9) and (10) are derived in the usual manner from the weak form of the governing equations (cf. Eqs. 1–4) with velocity and pressure degrees-of-freedom as the primary nodal variables. The geometric order of the element shape functions is quadratic in velocity and linear in pressure. Following discretization, the element matrices and vectors are assembled into a global system matrix and force vector in the usual manner resulting in the linear algebraic systems of equations:

$$\underline{KU} = \underline{F} \tag{11}$$

where $\underline{\underline{K}}$ is the global system 'stiffness' matrix, $\underline{\underline{U}}$ is the primary variable vector containing nodal velocities and pressures, and $\underline{\underline{F}}$ is the secondary variable vector containing 'load' terms and nodal reaction forces and flow rates. The solution technique used in computing the unknown velocities, pressures, and reactions at the nodes is based on partitioning the system matrix into essential 'e' and free 'f' degrees of freedom as:

 $^{^{1}}$ ψ_{n} here refers to streamline identifier (n) and starts at 1 from the left edge of the nozzle increasing transversely to a maximum number of 22 at the right edge of the nozzle.

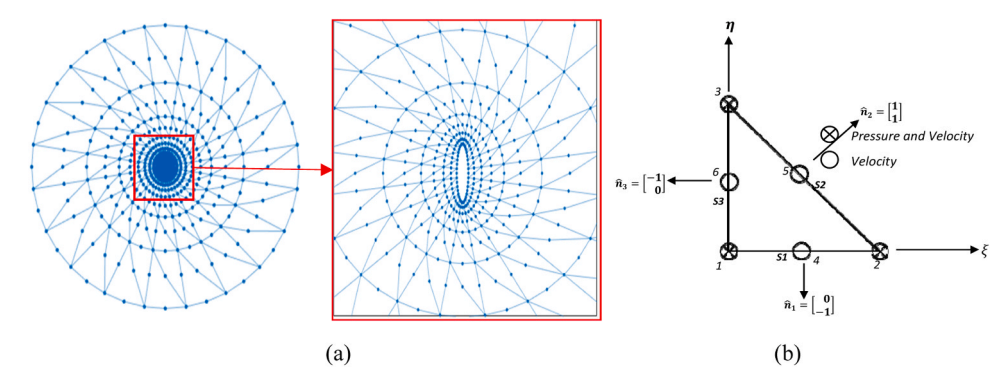


Fig. 6. Micro-model FEM: a) Fluid domain discretization b) Element selection with active dof.

$$\begin{bmatrix} \underline{\underline{K}}_{ff} & \underline{\underline{K}}_{fe} \\ \underline{\underline{\underline{K}}}_{ef} & \underline{\underline{K}}_{ee} \end{bmatrix} \begin{bmatrix} \underline{\underline{U}}_{f} \\ \underline{\underline{U}}_{e} \end{bmatrix} = \begin{bmatrix} \underline{\underline{F}}_{f} \\ \underline{\underline{F}}_{e} \end{bmatrix}$$
(12)

It follows that the unknown free velocities and pressure dofs in \underline{U}_f and unknown reactions forces and flowrates in \underline{F}_e from Eqs. 12 and 13 are computed, respectively, from:

$$\underline{U}_{f} = \underline{\underline{K}}_{f}^{-1} \left(\underline{F}_{f} - \underline{\underline{K}}_{fe} \underline{U}_{e} \right)$$
(13)

$$\underline{F}_{e} = \underline{K}_{af} \underline{U}_{f} + \underline{K}_{aa} \underline{U}_{e} \tag{14}$$

To compute the motion of a single fiber in the micro-model, the fiber's translational and angular velocities are obtained through an explicit numerical solution of the balance equations that zero the net hydrodynamic force and couple on the fiber's surface. The nonlinear solution of translational and rotational fiber velocities is achieved via Newton Raphson's iteration as:

$$\underline{\dot{X}}^{+} = \underline{\dot{X}}^{-} - \underline{J}^{-} \backslash \underline{R}^{-} \tag{15}$$

where $\underline{\dot{X}}$ contains the fiber velocities which includes the fiber center translational velocities $\underline{\dot{X}}_c$ and its angular velocity $\dot{\theta}$, i.e., $\underline{\dot{X}} = \begin{bmatrix} \underline{\dot{X}}_c & \dot{\theta} \end{bmatrix}^T$ and \underline{R} is the residual vector containing the fiber's hydrodynamic forces \underline{F}_H and couple M_H i.e., $\underline{R} = \begin{bmatrix} \underline{F}_H & M_H \end{bmatrix}^T$ which is a function of the fiber velocity, i.e., $\underline{R} = \underline{R}(\underline{\dot{X}})$. The '+' and '-' superscript refers to the current and previous iteration step of the Newton Raphson procedure. The fiber velocity vector is transformed from global to local reference frame according to the rotation matrix:

$$\underline{\underline{T}}_{\underline{\underline{X}}} = \begin{bmatrix} \underline{\underline{T}}_{\theta} & 0\\ 0^T & 1 \end{bmatrix} \tag{16}$$

such that

$$\underline{\dot{X}}' = \underline{\underline{T}}_{\underline{\dot{X}}}\underline{\dot{X}} \tag{17}$$

where variables on the local reference frame are accented with a superscript. The net force vector \underline{F}_H and couple M_H on the fiber's surface are calculated by vector summation of the nodal reactions forces and torques according to:

$$\underline{F}_{H} = -\sum_{k}^{N_{BC3}} \underline{F}_{e}^{(k)}, \ M_{H} = -\sum_{k}^{N_{BC3}} \underline{r}_{e}^{(k)} \times \underline{F}_{e}^{(k)}$$
(18)

where $\underline{r}^{(k)}$ is the position vector, $\underline{F}_e^{(k)}$ is the nodal reaction force vector at the k^{th} node on the fiber's surface (BC3), and N_{BC3} is the total number of nodes on BC3. The Jacobian J in Eq. 15 is computed by taking the

derivative of the components of the residual vector \underline{R} with respect to components of the fiber's velocity vector \dot{X} and is given as:

$$\underline{\underline{J}} = \frac{\partial \underline{R}}{\partial \underline{\dot{X}}} = \frac{\partial}{\partial \underline{\dot{X}}} \left[\underline{F}_H \quad \underline{\underline{M}}_H \right]^T = \left[-\sum_{k}^{N_{BC3}} \frac{\partial \underline{F}_e^{(k)}}{\partial \dot{X}} \quad -\sum_{k}^{N_{BC3}} \underline{r}_e^{(k)} \times \frac{\partial \underline{F}_e^{(k)}}{\partial \dot{X}} \right]^T \tag{19}$$

The derivative of the nodal reaction force vector is obtained using the chain rule and requires the differentiation of the partitioned stiffness matrices in Eq. (14) with respect to the fiber's velocity vector $\underline{\dot{X}}$ as:

$$\frac{\partial \underline{F}_{e}}{\partial \dot{\underline{X}}} = \frac{\partial \underline{\underline{K}}_{ef}}{\partial \dot{\underline{X}}} \underline{U}_{f} + \underline{\underline{K}}_{ef} \frac{\partial \underline{\underline{U}}_{f}}{\partial \dot{\underline{X}}} + \frac{\partial \underline{\underline{K}}_{ee}}{\partial \dot{\underline{X}}} \underline{U}_{e} + \underline{\underline{K}}_{ee} \frac{\partial \underline{\underline{U}}_{e}}{\partial \dot{\underline{X}}}$$
(20)

Similarly, using the chain rule, the derivative of the 'free' degrees-of-freedom \underline{U}_f with respect to the fiber's velocity \dot{X} is obtained by differentiating Eq. (13) as:

$$\frac{\partial \underline{\underline{U}}_{f}}{\partial \dot{\underline{X}}} = \underline{\underline{K}}_{ff}^{-1} \left(\frac{\partial \underline{F}_{f}}{\partial \dot{\underline{X}}} - \frac{\partial \underline{\underline{K}}_{ff}}{\partial \dot{\underline{X}}} \underline{\underline{U}}_{f} - \frac{\partial \underline{\underline{K}}_{fe}}{\partial \dot{\underline{X}}} \underline{\underline{U}}_{e} - \underline{\underline{K}}_{fe} \frac{\partial \underline{\underline{U}}_{e}}{\partial \dot{\underline{X}}} \right)$$
(21)

Upon consideration of Newtonian fluid model with solution-independent stiffness matrices and force vector (i.e., $\partial \underline{\underline{K}}/\partial \dot{\underline{X}}=0$ and $\partial \underline{F}_f/\partial \dot{\underline{X}}=0$), combining Eq. (20) and Eq. (21) yields:

$$\frac{\partial \underline{F}_{e}}{\partial \underline{\dot{X}}} = \left(\underline{\underline{K}}_{ee} - \underline{\underline{K}}_{ef} \underline{\underline{K}}_{fe}^{-1} \underline{\underline{K}}_{fe}\right) \frac{\partial \underline{\underline{U}}_{e}}{\partial \underline{\dot{X}}}$$
(22)

which is substituted into Eq. 18 to compute $\underline{\underline{J}}$. Given the fiber position and angle \underline{X}^j , and the fiber translational and rotational velocities $\dot{\underline{X}}^j$ at time step j the fiber location and angle at time step j+1 is updated based on an explicit fourth order Runge-Kutta method.

2.3. Validation of micro-model simulation approach

Jeffery [32] derived an analytical solution for the motion of an ellipsoidal particle in a purely viscous Newtonian fluid through linearization of the Navier-Stokes equations. The derivations by Jeffery were an extension of the earlier work of Oberbeck [30] and Edwardes [31] who in given order, developed the equations of motion for an ellipsoid in viscous fluid translating along and rotating about one of its principal axes. The extent of validity to Jeffery's derivations is limited to the assumption of low Reynold's number creeping flows. Jeffery assumed the particle center travels with the same velocity as the undisturbed fluid and rotates due to shear and distortion of the surrounding fluid (cf. Fig. 7). The equations for the particle's motion were derived from equilibrium equations of the resulting forces and torque acting on the particle by the action of the surrounding fluids pressure on the particles surface which were found to be periodic and dependent on the particle's initial orientation. Jeffery assumed laminar incompressible, purely

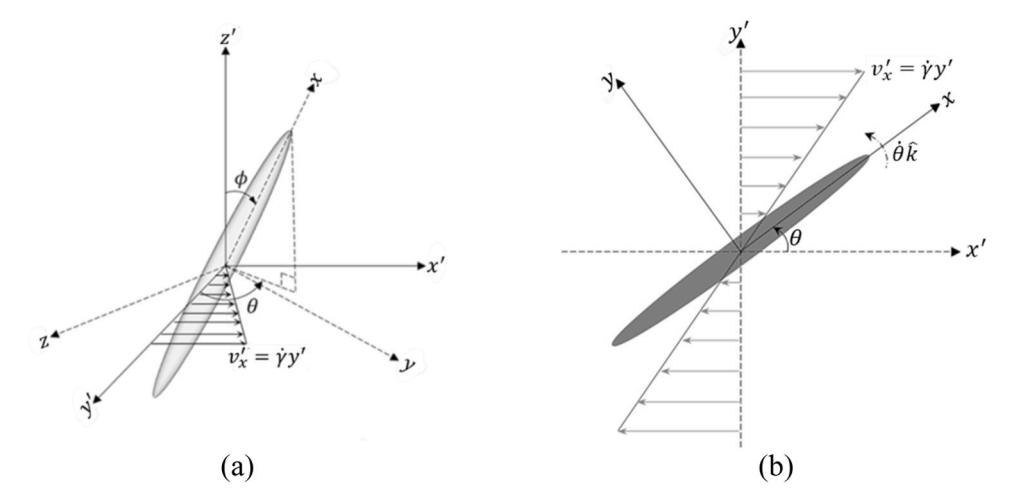


Fig. 7. Fiber orientation angles: a) 3D coordinates used in fiber orientation tensor equations and b) 2D coordinates used in single fiber motion simulations.

viscous, simple shear flow with a Newtonian fluid for the particle suspension (i.e., $\mu = constant$ and $v_y^{'} = v_z^{'} = 0$, $v_x^{'} = \dot{\gamma}\dot{y}$.(cf. Fig. 7). By assuming an average far-field pressure $p_0 = 0$, for the undisturbed flow, he obtained an expression for the particle's in-plane orientation θ and angular velocity $\dot{\theta}$ given respectively by [47].

$$\theta(t) = \tan^{-1}\left(\sqrt{(1+\xi)/(1-\xi)}\tan\left\{(\dot{\gamma}/2)\sqrt{1-\xi^2}\,t\right\}\right) \text{ and } \dot{\theta}(t)$$

$$= (\dot{\gamma}/2)[\xi\cos 2\theta + 1] \tag{23}$$

where ξ is the particle shape parameter given by $\xi = (r_e^2 - 1)/(r_e^2 + 1)$ and $\dot{\gamma}$ is the shear rate. The particle's orbital period for complete tumbling is given as [47].

$$t_p = 4\pi / \dot{\gamma} \sqrt{1 - \xi^2} \tag{24}$$

Jeffery [32] also derived a solution for fluid pressure from the Laplace equation which can be expressed in Two-Dimensional (2D) form as:

$$p = p_0 + 2\mu \left\{ A \frac{\partial^2 \Omega}{\partial^2 x} + B \frac{\partial^2 \Omega}{\partial^2 y} + (H + H') \frac{\partial^2 \Omega}{\partial x \partial y} \right\}$$
 (25)

Definition for the Laplace Function $\Omega\&\Delta$ and derivations for the constants A.B.H.H. based on the 2D contraction can be found in

Appendix II.

After choosing an appropriate fluid domain size such that the boundary BC1 is sufficiently far from the fiber surface (cf. Figs. 5b and 6a), computed results using our FEM micro-model with simple shear flow of a fiber's in-plane orientation and rotational velocity are in good agreement with Jeffery's analytical solution in Eqs. (22) through (25) for a single complete tumbling period as shown in Fig. 8.

Fig. 9 shows the evolution of the maximum and minimum pressure on the fiber surface over the tumbling period from Jeffery's (blue) and FEA simulation (red) results. A periodic drop and subsequent increase by a magnitude of about 8kPa relative to the mean reference pressure is seen which supports our hypothesis on the occurrence of low-pressure sites along Jeffery's orbit and suggests a propensity for void nucleation at these orientations. Upon comparing Figs. 8 and 9, it can be seen that the extreme point of low pressure occurs as the fiber rotates towards alignment in the direction of fluid flow. The location of the pressure extremes varies from point to point on the fiber's surface during its motion along Jeffery's orbit. As a result, the pressure extreme depends on the mesh refinement on the fiber surface which results in minor discrepancies observed between the extreme pressure profiles obtained from Jeffery's exact solution and FEA simulation in Fig. 9a. We however see that the pressure evolution on the fiber tip match closely (Fig. 9b).

Vaxman et al. [6] noted that the fiber geometry, operating condition and the fluid rheological properties are important factors that influence

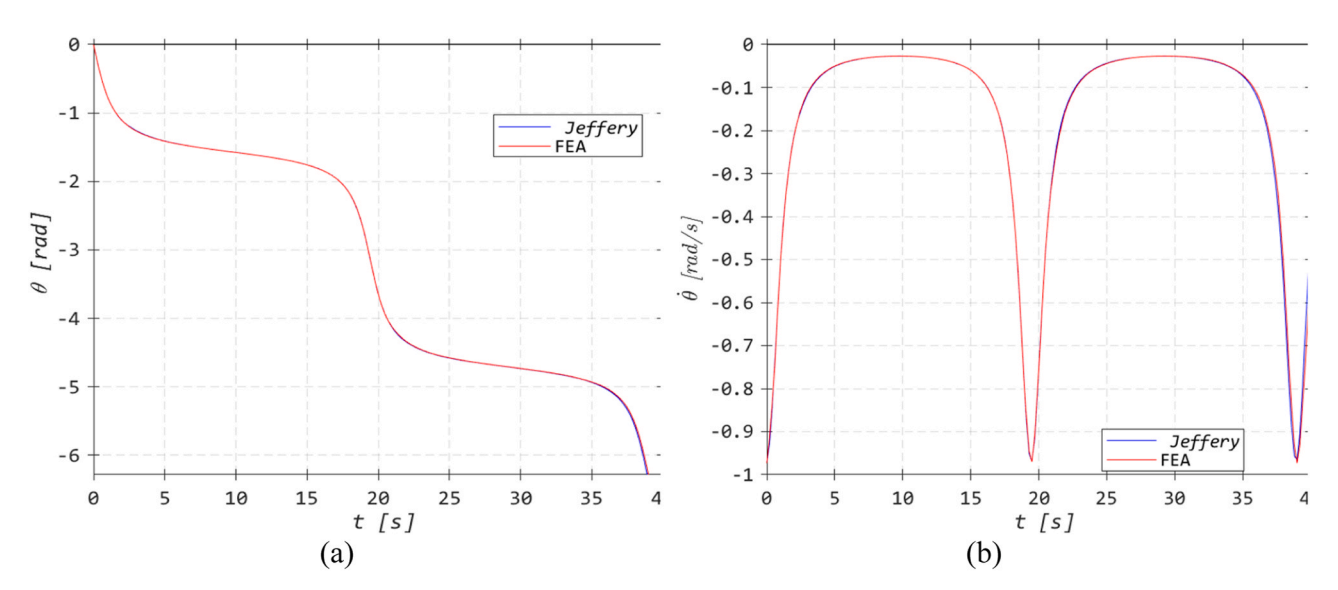


Fig. 8. Fiber's in-plane orientation angle (a) and angular velocity (b) and for the FEA simulation (red) and Jeffery's Solution (blue).

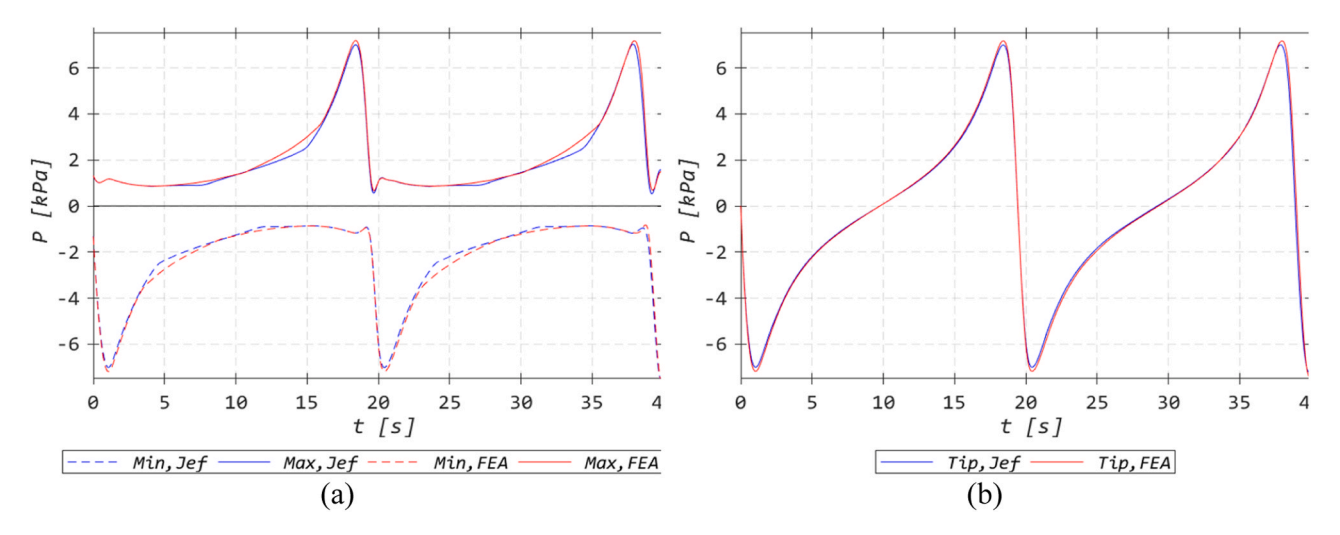


Fig. 9. (a) Fiber surface maximum (continuous lines) and minimum (dashed lines) pressure (b) fiber tip pressure, evolution along Jeffery's orbit for both FEA simulation (red lines) and Jeffery's solution (blue lines).

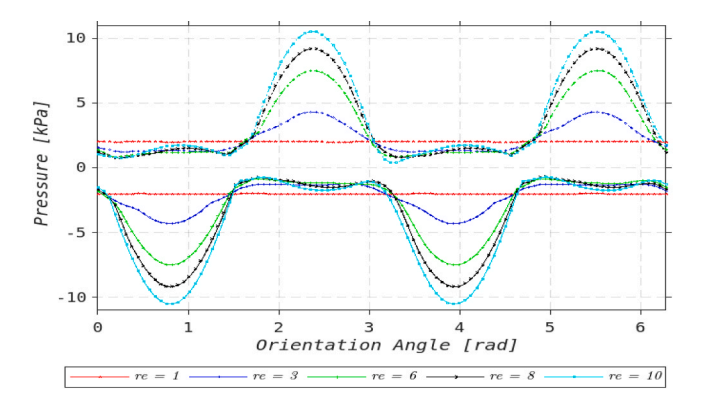


Fig. 10. Maximum (upper curves P > 0) and minimum (lower curves P < 0) fiber surface pressures for various aspect ratio in simple shear flow $(\dot{\gamma} = 1s^{-1})$.

void formation. To better understand this relationship, we performed sensitivity analysis on the fiber's geometric aspect ratio r_e which shows that the magnitude of r_e varies directly with the max and min pressures on the fiber's surface as it rotates through Jeffery's orbit in simple shear flow [48]. Fig. 10 illustrates that the minimum pressure on the fiber surface drops as the shape of the ellipsoid oblates from a prolate spheroid to a perfect sphere at which point there are no noticeable pressure peaks on the fiber surface during its evolution, as expected. A closer inspection of the pressure contour plots appearing in Fig. 11 shows the location of minimum pressure on the fiber surface and that these low-pressure sites occur at the fiber tip consistent with the conclusion of Vaxman et al. [6].

The shear rate magnitude and Newtonian viscosity is observed to influence computed pressure response as that for fiber aspect ratio, i.e.,

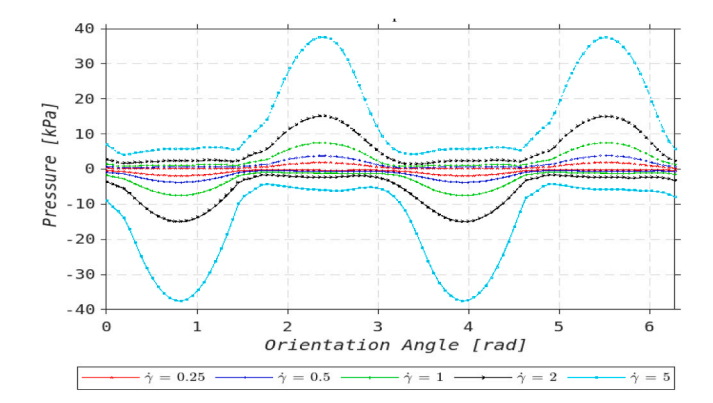


Fig. 12. Maximum (upper curves P > 0) and minimum (lower curves P < 0) fiber surface pressures for various shear rate values in simple shear flow (re=6). The units for γ are s-1.

higher shear rate and viscosity result in a higher peak pressure at sites where they occur on the fiber surface as shown in Figs. 12 and 13. These factors (fiber aspect ratio, viscosity, and flow shear rate), however, affect Jeffery's period differently. While the period is observed to vary directly with aspect ratio (i.e., implying faster tumbling for shorter fibers) the reverse is the case with the shear rate magnitude (cf. Table 1) which varies inversely with the period as higher shear rate results in higher fiber angular velocities, as predicted by Jeffery. However, Jeffery's period is unaffected by the viscosity magnitude. In summary, higher geometric aspect ratios, shear rate magnitude and viscosity result in lower fiber surface pressure drops, thus an increase in these factors provide favorable conditions that increase the propensity for voids to nucleate for suspended fibers in simple shear flow.

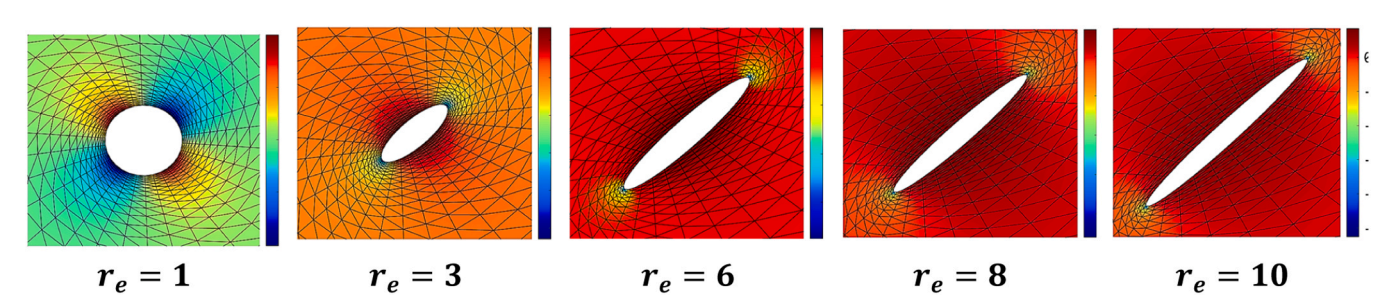


Fig. 11. Pressure distribution around fiber's surface for at the point of minimum pressure drop for different fiber's aspect ratio.

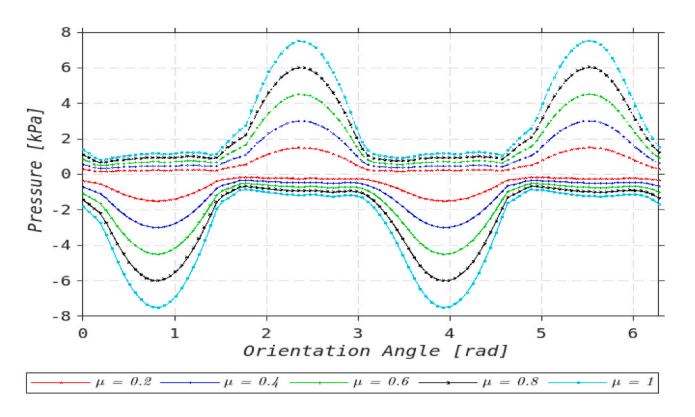


Fig. 13. Maximum (upper curves P > 0) and minimum (lower curves P < 0) fiber surface pressure limits for various Newtonian viscosities in simple shear flow ($r_e = 6$). The units for μ are $Pa \bullet s$..

Table 1
Table comparing period of fibers tumbling motion obtained from Jeffery's approximation to FEA calculations for various aspect ratio and shear rate.

| r _e | T_{Jef} [s] | $T_{fea} \ [s]$ | $\dot{\gamma} \ [1/s]$ | T_{Jef} [s] | T_{fea} [s] |
|----------------|---------------|-----------------|------------------------|---------------|---------------|
| 1 | 12.57 | 12.87 | 0.25 | 154.99 | 157.49 |
| 3 | 20.94 | 21.24 | 0.5 | 77.49 | 78.76 |
| 6 | 38.75 | 39.53 | 1 | 38.75 | 39.53 |
| 8 | 51.05 | 52.32 | 2 | 19.37 | 19.99 |
| 10 | 63.46 | 65.34 | 5 | 7.75 | 7.89 |

2.4. Non-dilute fiber suspension motion

Jeffery's model assumes a Newtonian fluid and is valid for dilute suspension where fibers possess a relatively large radius of influence with neighboring fibers and contribute independently to the dissipation of energy in the form of a modified isotropic effective fluid viscosity μ^* for the suspension, such that $\mu^* = \mu$ $(1 + \kappa \vartheta_f)$ [32], where κ is the modification factor dependent on the particles dimension which has been accounted for in our extrusion-deposition macro-model appearing above and ϑ_f is the volume fraction of the ellipsoidal fiber in the suspension. However, for semi-dilute and concentrated suspensions, there exists some degree of stochasticity in an individual fiber's behavior due to momentum diffusion and fiber-fiber interactions as the distance between neighboring particles becomes small relative to its size. In this case, neighboring fibers would introduce some degree of disturbance in a particle's surrounding fluid. As a result, particle-particle interaction necessitates a coupling effect between fibers. In other words, interactions between fibers reduce the effective radii of influence between near neighbors, the proximity of which results in an increased energy dissipation within each fiber's sphere of influence [40,41].

As the fiber volume fraction and/or aspect ratio increases, collision of particles creates momentum transfer between colliding particles. Kugler et. al [40] classified fiber-fiber interaction into long-range and short-range hydrodynamic interaction, the latter of which can be further sub-divided into short range lubrication regimes, direct mechanical contact and a transition regime. As a result of momentum diffusion, the fibers eventually assume a steady state orientation that depends on the initial condition in accordance with the indeterminacy described by Jeffery. Folgar and Tucker [49] extended Jeffery's analysis by accounting for a collection of interacting suspended particles by incorporating a rotary diffusion term D_r . The rotary diffusion term D_r is defined in terms of the scalar magnitude of deformation tensor $\dot{\gamma}$ according to D_r $= C_I \dot{\gamma}$, where C_I is the interaction coefficient which is an empirical constant. Kugler et. al [40] gives a review of existing orientation models that accounts inter-particle interaction such as nematic model, anisotropic and mold flow rotary diffusion model, retarding principal rate

model, etc.

To capture fiber-fiber interactions in our single fiber model, we develop a relation between the Folgar-Tucker interaction coefficient C_I and the effective radius of influence in our micro-model. Firstly, we determine a relation between the stall angle of the fiber and the interaction coefficient C_I based on equation of change of the 2nd order orientation tensor by Advani and Tucker [50]. Here the stall angle is the fiber angle at which rotary motion ceases which has been found to be a function of the micro-model flow domain size (see e.g., Zhang et al. [40]). Subsequently we obtained a relation between the flow domain size and the fiber stall angle through a series of micro-model FEA simulations with fluid boundary domain BC1 of different sizes. As M decreases, the ends of the fiber become nearer to the prescribed boundary BC1 such that the velocity field near the fiber tips hydrodynamically interacts with the flow adjacent to BC1. The prescribed boundary creates a flow disturbance as viewed from the fiber in a manner similar to that which would be expected by neighboring fibers in a semi-concentrated flow. We then determine the relationship between the steady-state orientation tensor and the interaction coefficient C_I for a given ellipsoidal aspect ratio. A relationship between C_I and the micro-model flow domain size is then established by equating fiber stall angle in the micro-model to the direction of the first eigenvector of the fiber orientation tensor at steady state. This approach provides a means to approximately account for the effect of fiber-fiber interaction in the FEA simulation of the single fiber evolution along streamlines for a given interaction coefficient.

Observations of the experimentally determined steady state orientation [51] show that the fibers tend to align with streamlines of the flow field irrespective of the initial conditions, contrary to Jeffery's idealization where suspended particles continue to rotate in simple shear. Saffman [51] shows that non-Newtonian properties of the fluid, not considered by Jeffery, is responsible for a stall in the tumbling motion. Other factors not accounted for in Jeffery's model that adds to the indeterminacy of a particle's motion include the flexural tendency of the particle which would depend on its inherent elastic property, aspect ratio, fluid rheology of the medium and interacting flow field. Moreover, the fibers may eventually break when subject to severe interacting forces, however, fiber flexibility is beyond the scope of our work.

2.5. Determining effective fluid domain size

To quantify the effect of fiber-fiber interactions with our single fiber model, we first establish a relationship between a suspension's interaction coefficient C_I (cf. the Advani-Tucker model) and the stall angle in our single fiber FEA micro-model. The steady state orientation tensor values that correspond to a particular interaction coefficient can be determined from the Advani-Tucker 2nd order orientation tensor equation of change given as:

$$\dot{\mathbf{a}}_{ij} = \frac{1}{2} \left(\omega_{im} \mathbf{a}_{mj} - \mathbf{a}_{im} \omega_{nj} \right) + \frac{\xi}{2} \left(\Gamma_{im} \mathbf{a}_{mj} + \mathbf{a}_{im} \Gamma_{mj} - 2 \mathbf{a}_{ijkl} \Gamma_{kl} \right) + 2 D_r \left(\delta_{ij} - \alpha \mathbf{a}_{ij} \right)$$
(26)

where, a_{ij} and a_{ijkl} are the 2nd and 4th order fiber's orientation tensors, respectively, ξ is the shape parameter defined above, Γ_{ij} is the strain rate tensor given as $\Gamma_{ij} = \left[\nabla_i v_j + \nabla_j v_i \right]$, ω_{ij} is the vorticity tensor given as $\omega_{ij} = \left[\nabla_i v_j - \nabla_j v_i \right]$ and α is a dimension factor (i.e., $\alpha = 3$ for 3D orientation and $\alpha = 2$ for 2D planar orientation). In the above, the fourth-order orientation tensor a_{ijkl} is computed from a_{ij} using a closure approximation as is common in polymer composite suspension simulations. We employ the orthotropic fitted closure of Verweyst et al. [52] in all the calculations to follow. The symmetry properties of the orientation tensors require that $a_{ij} = a_{ji}$ and $a_{ijkl} = a_{kijl} = a_{klij}$. The normalization condition also requires that $a_{ii} = 1$ and $a_{ijkk} = a_{ij}$ where repeated indices imply summation in the usual manner here and in the following.

We determine the steady state 2nd order orientation tensor that results in zero rate of change, i.e., $\dot{a}_{ij}=\theta$ via a Newton Raphson iteration scheme given as:

$$a_{ij}^{+} = a_{ij}^{-} - J_{mnij}^{-} \backslash R_{mn}^{-}$$
 (27)

where the residual $R_{mn} = \dot{a}_{mn}$ is:

$$R_{mn} = \frac{1}{2}(\omega_{mk}a_{kn} - a_{mk}\omega_{kn}) + \frac{\xi}{2}(\dot{\gamma}_{mk}a_{kn} - a_{mk}\dot{\gamma}_{kn} - 2\dot{\gamma}_{kl}a_{mnkl}) + 2D_r(\delta_{mm} - \alpha a_{mn})$$
 (28)

and the Jacobian J_{mnij} is obtained by differentiating the residual with-respect-to components of the 2nd order orientation tensor a_{ij} as.

$$\begin{split} I_{mnij} &= \frac{\partial R_{mn}}{\partial a_{ij}} \\ &= \frac{1}{2} \left(\omega_{mk} \frac{\partial a_{kn}}{\partial a_{ij}} - \frac{\partial a_{mk}}{\partial a_{ij}} \omega_{kn} \right) + \frac{\xi}{2} \left(\dot{\gamma}_{mk} \frac{\partial a_{kn}}{\partial a_{ij}} \right. \\ &+ \frac{\partial a_{mk}}{\partial a_{ij}} \dot{\gamma}_{kn} - 2 \dot{\gamma}_{kl} \frac{\partial a_{mnkl}}{\partial a_{ij}} \right) - 2 D_r \alpha \frac{\partial a_{mn}}{\partial a_{ij}} \end{split}$$
(29)

The derivative of the 2nd order orientation tensor with respect to its

individual components is simply:

$$\frac{\partial a_{rs}}{\partial a_{mn}} = \delta_{rm} \delta_{sn} \tag{30}$$

where δ_{ij} is the Kronecker delta. Derivatives of a_{ijkl} with respect to a_{ij} are provided elsewhere for various closures approximations that are commonly used with Eq. (26) (cf. Awenlimobor and Smith [53], to appear). We define a preferred direction of orientation as the principal direction of the steady state a_{ij} computed from the n^{th} eigenvector of $a_{ij}(\Phi_{mn})$ corresponding to the maximum eigenvalue λ_n which is obtained from:

$$\underline{\boldsymbol{\Phi}}: \Lambda_{ij} = \boldsymbol{\Phi}_{ki} \mathbf{a}_{kn} \boldsymbol{\Phi}_{nj}, \ \lambda_k = \Lambda_{kk}, \ \underline{\lambda}: \epsilon_{ijk} \left[\mathbf{a}_{ij} - \lambda_n I_{ij} \right] = 0 \tag{31}$$

Consider planar simple shear flow having $v_x' = \dot{r}y'$ and $v_y' = v_z' = 0$ (cf. Fig. 7) with a fiber at $\phi = 90^\circ$ rotating in the xy-plane. For this flow field, the in-plane steady state orientation angle θ was evaluated using Eqs. (26) through (31) for various values of C_I and for different closure approximations as given in [53]. Alternatively, a series of FEA simulations were performed for an ellipsoidal fiber rotating through a modified Jeffery's orbit in simple shear for various fluid boundary domain sizes

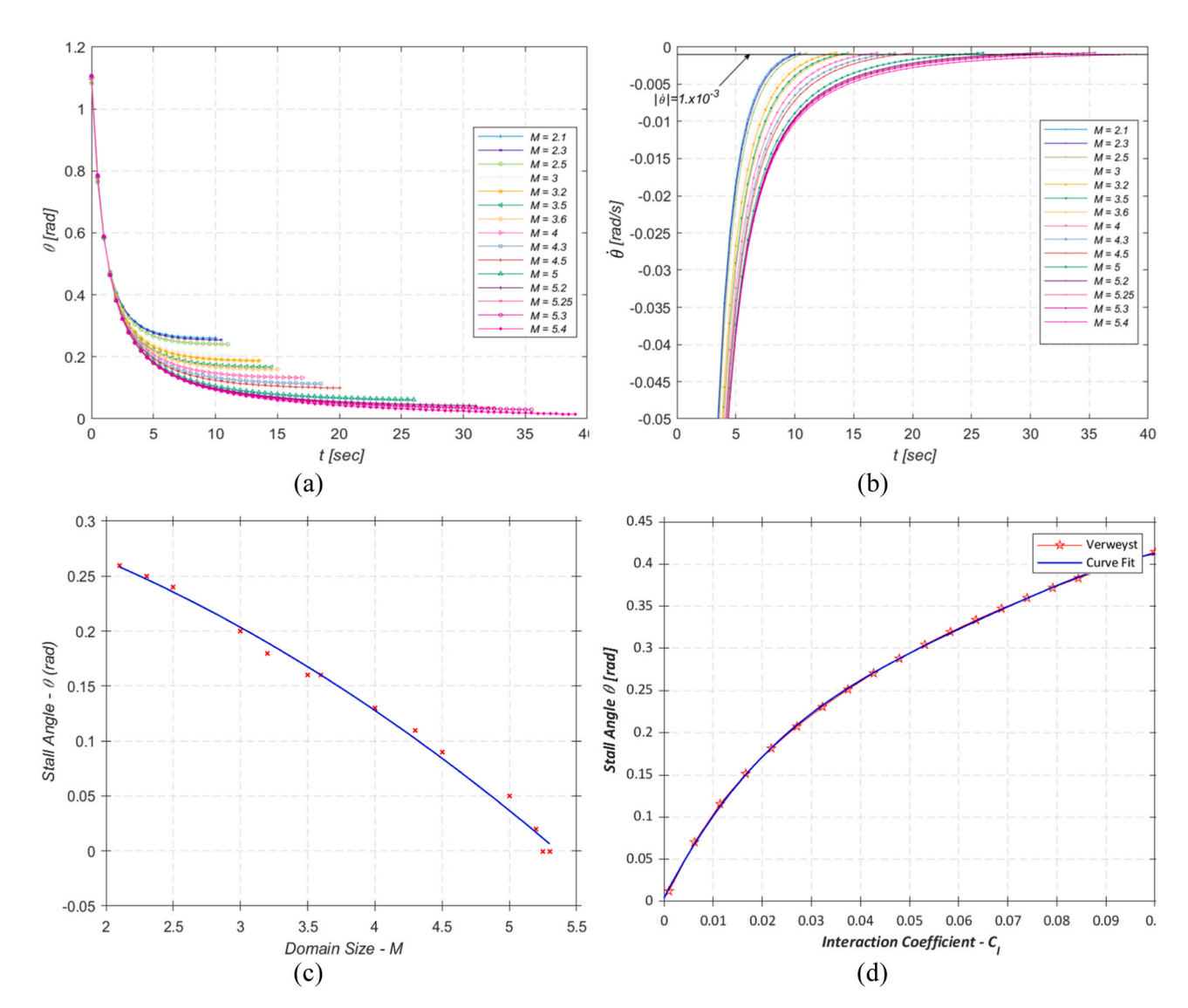


Fig. 14. Single fiber angular motion and preferred orientation results for varying domain size M a) fiber orientation angle θ through its stall angle b) fiber angular velocity $\dot{\theta}$ simulated through a stall angular velocity tolerance of $\left|\dot{\theta}\right| = 1. \times 10^{-3} 1/s$ c) relationship between fiber stall angle and domain size factor M from FEA analysis, d) relationship between fiber steady state angle θ and interaction coefficient C_I (Aspect ratio $r_e = 6$).

(cf. Fig. 5). A corresponding pair of FEA simulation and orientation tensor evaluations were performed using the same fiber geometry and shear rate. Values of stall angle were then compared. Results of stall angle as a function of micro-model domain size factor M=2d/a (where d is the diameter of the micromodel flow domain) and C_I appear in Fig. 14.

The influence of domain size appearing in Fig. 14c shows a nearly linear relationship between the fiber stall angle and domain size from the micro-model simulations, given by Eq. (32) below.

$$\theta = .33839 - .022M - .0077M^2 \tag{32}$$

Additionally, results of the orientation angle computed from the eigenvectors of the steady state orientation tensor \mathbf{a}_2 show nonlinear relationship between stall angle and interaction coefficient (cf. Fig. 14d) which can be represented as:

$$\theta = \pi/2 - 1.57 + 11.4C_I - 183.5C_I^2 + 1773.4C_I^3 - 6680.1C_I^4$$
(33)

Combining results from Fig. 14c and Fig. 14d, we obtain a relationship between the fluid boundary domain size in our single fiber micromodel and $C_{\rm I}$ given as (cf. Fig. 15)

$$M = -1.4285$$

$$+\sqrt{45.89 - 1.48 \times 10^{3} C_{I} + 2.38 \times 10^{4} C_{I}^{2} - 2.30 \times 10^{5} C_{I}^{3} + 8.68 \times 10^{5} C_{I}^{4}}$$

Assuming an ellipsoidal fiber aspect ratio $r_e=6$ which corresponds to a shape parameter $\xi=0.9459$ and given a volume fraction $\vartheta_f=8.4\%$ by volume (13% by weight) CF/ABS polymer composite, we obtain an interaction coefficient of $C_I=0.0128$ using Bay's correlation that relates C_I to ϑ_f and r_e [54]. It follows from Eq. (34), that the effective domain size based on our C_I is $M=4.08(\sim4.0)$ which we have used in our simulations. Given that fiber suspensions are classified into 3 concentration regimes based on v_f and r_e as [37]:

$$\begin{cases} \theta_f < \frac{1}{r_e^2} & dilute \\ \frac{1}{r_e^2} \le \theta_f < \frac{1}{r_e} & semi - dilute \\ \theta_f < \frac{1}{r_e^2} & concentrated \end{cases}$$
(35)

our simulations are within or nearly within the concentrated regime for the suspension where $C_I = .0128$ and M = 4 are used in the results section below.

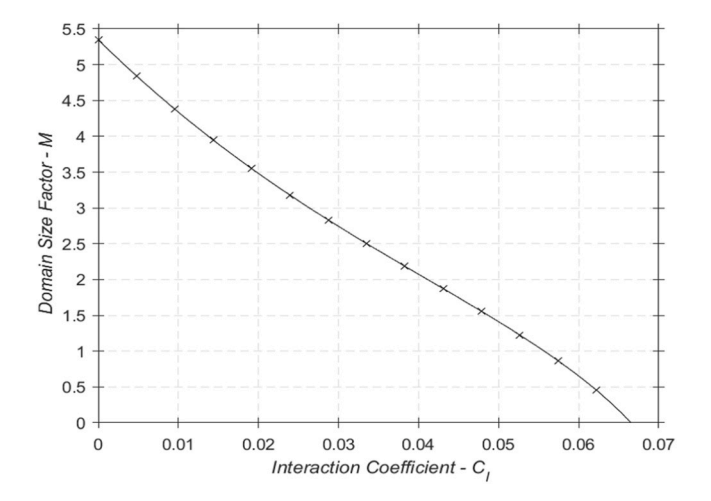


Fig. 15. Fitted relationship between domain size factor M vs interaction coefficient C_I .

3. Results and discussion

The preceding sections describe the ability of our micro-model to reproduce Jeffery's result for single fiber motion, and the determination of an effective single ellipsoidal fluid domain size that approximates the effect of short-range fiber interaction in simple shear flow. All simulations included here use a fiber half-length of $a = 42\mu m$ and an ellipsoidal aspect ratio of $r_e = 6$ which corresponds to a cylindrical geometric aspect ratio of $r_c = 7.66$ using Equation (2.21) in Zhang [41]. Here we limit our discussion to results along streamlines $\psi_4,\,\psi_{10},$ and ψ_{18} to capture effects along the lower, middle, and upper sections of the bead, respectively (cf. Fig. 2b). The following simulations incorporate velocity, velocity gradients, and pressure computed in the 2D planar extrusion-deposition macro-model to define far field boundary conditions BC1 and BC2 in the single fiber micro-model. To assess the effect of initial conditions in the single fiber analysis, we run multiple simulations, each with its own initial fiber angle θ_0 over a range of $-\pi/2 \le \theta_0 \le \pi/2$ in increments of $\pi/12$. Simulating fiber motion over this range of initial angles and on various streamlines provides a comprehensive assessment of possible fiber responses and corresponding location where they occur across the extruder nozzle.

To better display streamline results, subsequent figures presented in this section have been annotated to show three interest regions of the nozzle geometry appearing in Fig. 2b which includes:

- (i) Zone 1: The entrance to the small capillary section of the nozzle at the point where the polymer- melt just exits the convergent zone.
- (ii) Zone 2: The exit from the nozzle where the polymer leaves the nozzle and enters the region of die swell, and the external pressure drops to atmospheric condition.
- (iii) Zone 3: The exit of die swell region below and to the side of the nozzle exit where the deposited material has made a complete 90° turn onto the translating bed below and attains a near uniform velocity equal to the print speed.

We consider the simulation of fibers in a concentrated suspension with $C_I = 0.0128$ using the reduced single fiber domain approach with M = 4 in the micro-model as described above. For each fiber motion simulation result (i.e., a fiber moving along a specific streamline with a designated initial angle), the overall minimum and maximum fiber surface pressure is calculated and the difference between the streamline pressure and overall minimum and maximum fiber surface pressures are noted. In addition, the corresponding coordinate locations where the minimum and maximum fiber surface pressures occur within extrusiondeposition flow are identified. Fig. 16 shows a typical fiber surface pressure result along streamline ψ_{10} (starting at the centerline of the nozzle inlet) for a concentrated suspension where distinct extremes of minimum and maximum pressures identified as ΔP_{\min} and ΔP_{\max} , respectively, are plotted as a function time along with the streamline pressure from the macro-model. The first extreme pressure location, denoted here as Loc. 1, and the second extreme location, denoted as Loc. 2, appear in the pressure history for all streamlines and θ_0 with varying degrees of intensity and at slightly different locations as shown below. Note that the position along the streamline for Loc. 1 and Loc. 2 will occur at different locations depending on the streamline and initial fiber angle.

The initial extreme in minimum fiber surface pressure at Loc. 1 is observed to occur just prior to the entrance of the nozzle capillary section (i.e., zone 1) while the second pressure drop at Loc. 2 occurs within the die swell region between zones 2 & 3. Only at the latter extreme fiber location does the absolute local minimum pressure on the fiber surface drop to a value that is below zero atmosphere (reaching $-0.4 \, MPa$ in the simulation appearing in Fig. 16). This low pressure extreme is expected to provide a favorable condition for void nucleation to occur based on prior related research [11–17]. A closer inspection of the fiber's surface

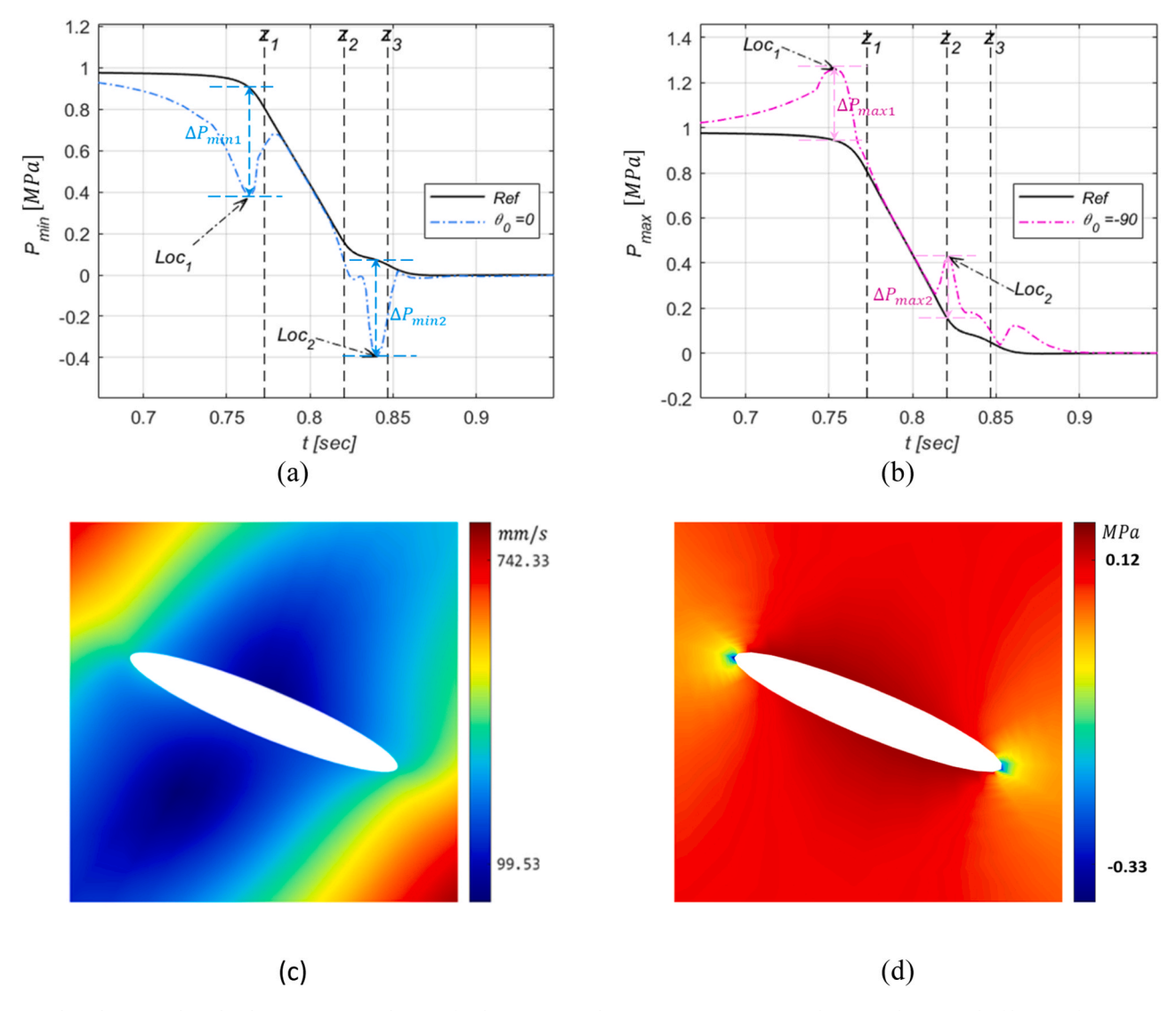


Fig. 16. Selected computed results along center streamline ψ_{10} for the concentrated suspension ($C_I = 0.0128$ and M = 4). Shown are the fiber's surface (a) minimum pressure ($\theta^0 = 0^0$) (b) maximum pressure ($\theta^0 = -90^0$) at peak locations (Loc. 1 & Loc. 2). Contour plot at the first location (Loc. 1) of minimum pressure drop showing (c) Velocity magnitude (d) Pressure near the fiber.

pressure distribution at this location shows that the peak sites occur at the fiber's tips (cf. Fig. 16d) which is typical of all simulations presented in this work

To gain a better understanding of the effect of streamline location on the fiber response during its motion through the extrusion-deposition flow in the concentrated regime, we present results of time-varying profiles for three select streamlines, one near the left edge - ψ_4 , the center streamline - ψ_{10} , and one at the far-right edge ψ_{18} (cf. Fig. 2b), each with a range of initial fiber orientation as specified above. The computed results show that the fiber surface extreme pressures on the outer streamlines (ψ_4 and ψ_{18}) are less sensitive to initial fiber orientation over the entire deposition time as compared to the center streamline ψ_{10} where the initial fiber angle has much more pronounced effect on the characteristic pressure peak values.

The results of the fiber orientation relative to the streamline direction presented in Fig. 17 shows that the particle eventually tends to align with the streamlines of the flow irrespective of its initial starting angle and the degree of fiber alignment increases from the center streamline (ψ_{10}) to streamlines closer to edges of the nozzle $(\psi_4 \quad \text{and} \quad \psi_{18})$. The asymmetry in the results of the orientation for edge streamlines $\psi_4 \ll \psi_{18}$ shown in Fig. 17 a and c, respectively, signifies that fibers on these

streamlines undergoes uneven rotation prior to flow alignment depending on the degree and direction of initial misalignment relative to the prevailing vortex direction (ω) of the undisturbed flow which in turn depends on the relative positioning of the streamline with respect to the centerline.

To better depict the fiber rotation span for fibers initially inclined unfavorably with the flow, the orientation transient profiles have been vectorially added to π considering the fiber has no preferred ends (i.e., $\theta(t) = -\theta(t) - \pi$, $\theta_0 < 0$, $\omega > 0$ for streamline ψ_4 and $\theta(t) = -\theta(t) + \pi$, $\theta_0>0, \ \ \omega<0$ for streamline ψ_{18}). Alternatively, the fiber motion on the outer streamlines is more sensitive to the initial fiber orientation and possesses some degree of asymmetry with respect to the initial angle. This is due to the relatively high velocity gradients for streamlines closer to the nozzle edge as compared to the center streamline. Moreover, the transition time in the die swell region between zones 2 and 3 increases with streamline location from the right-hand edge to the left-hand edge due to correspondingly larger radius of curvature (cf. Fig. 2b). Streamline 18 has a sharp 90° turn with negligible dwell time in the die swell region as zones 2 and 3 almost nearly overlaps unlike streamline 4 and 10 which experiences relatively higher dwell in the die swell region as the polymer melt gradually approaches the deposition plate surface.

For subsequent simulation results, we consider a range of initial fiber

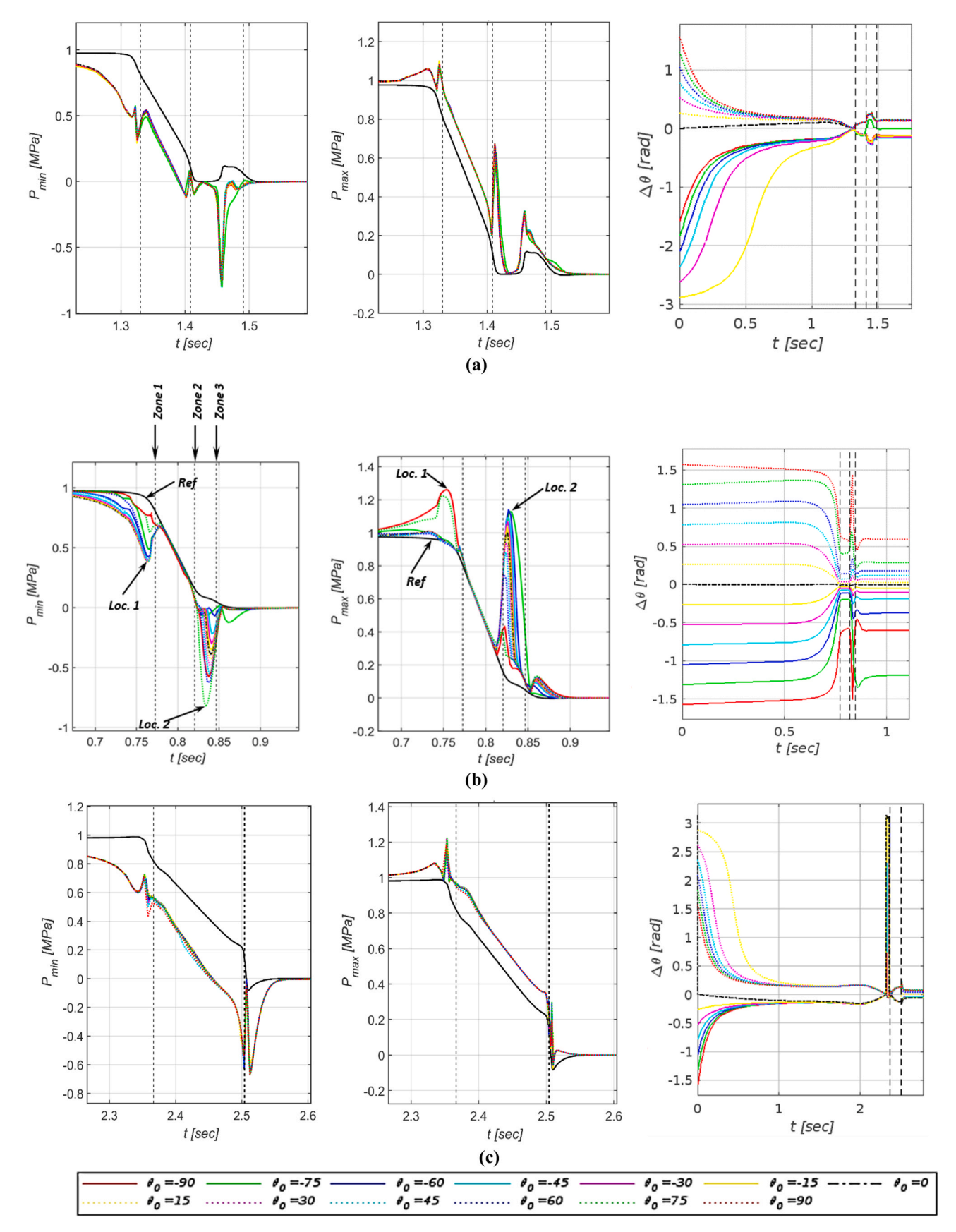


Fig. 17. Quasi-transient profile plots of the fiber minimum pressure, maximum pressure and relative orientation angle, including various initial fiber angles for selected streamlines a) streamline-10 and c) streamline-18 ($C_I = 0.0128$ and M = 4).

orientation and report the computed overall minimum and maximum pressure difference with respect to the streamline pressure across the nozzle at the important extreme pressure locations (i.e., Loc. 1 and 2). In addition, we report the corresponding spatial positions where the minimum and maximum pressure extremes occur within extrusion-deposition flow for each of the various streamlines across the nozzle section. Lastly, we report the fiber's orientation relative to the streamline direction at three interest zones of the nozzle (zones 1–3).

Calculated results in Fig. 18 show that the extreme pressures on center streamlines are more sensitive to initial fiber angle than that for the outer streamlines. We observe a drop in average minimum pressure

of -0.5 MPa at the first extreme occurrence (Loc. 1) which is almost uniform across all streamlines within the nozzle. Alternatively, the second average pressure extreme occurrence (Loc. 2) has a minimum streamline pressure of -0.8 MPa at the left edge streamline and -0.1 MPa at the right edge (cf. Fig. 18b). The spatial position where the first extreme in the minimum pressure drop occurs across the nozzle is seen to be well-above the entrance to the straight nozzle capillary (zone 1) but at the second pressure extreme location, the mean minimum extreme pressure occurs across the die swell region of the flow as shown in Fig. 19b. This would indicate that the likelihood of void nucleation decreases from the bottom to the upper free surface of the bead. The

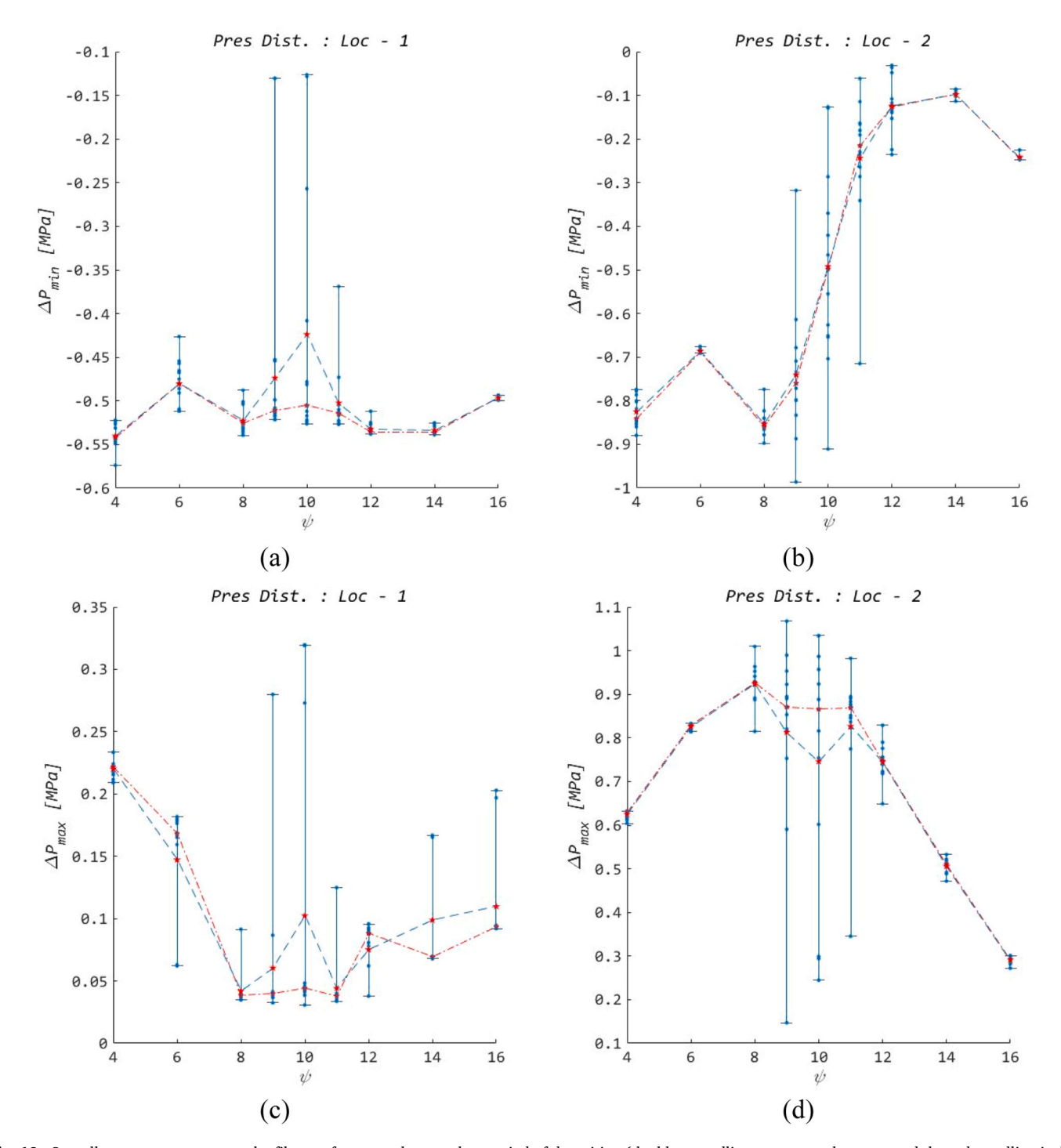


Fig. 18. Overall pressure extremes on the fiber surface over the complete period of deposition (the blue trendline represents the mean and the red trendline is the median): (a) overall minimum at Loc. 1 (b) overall minimum at the Loc. 2 (c) overall maximum at Loc. 1 (d) overall maximum at Loc. 2.

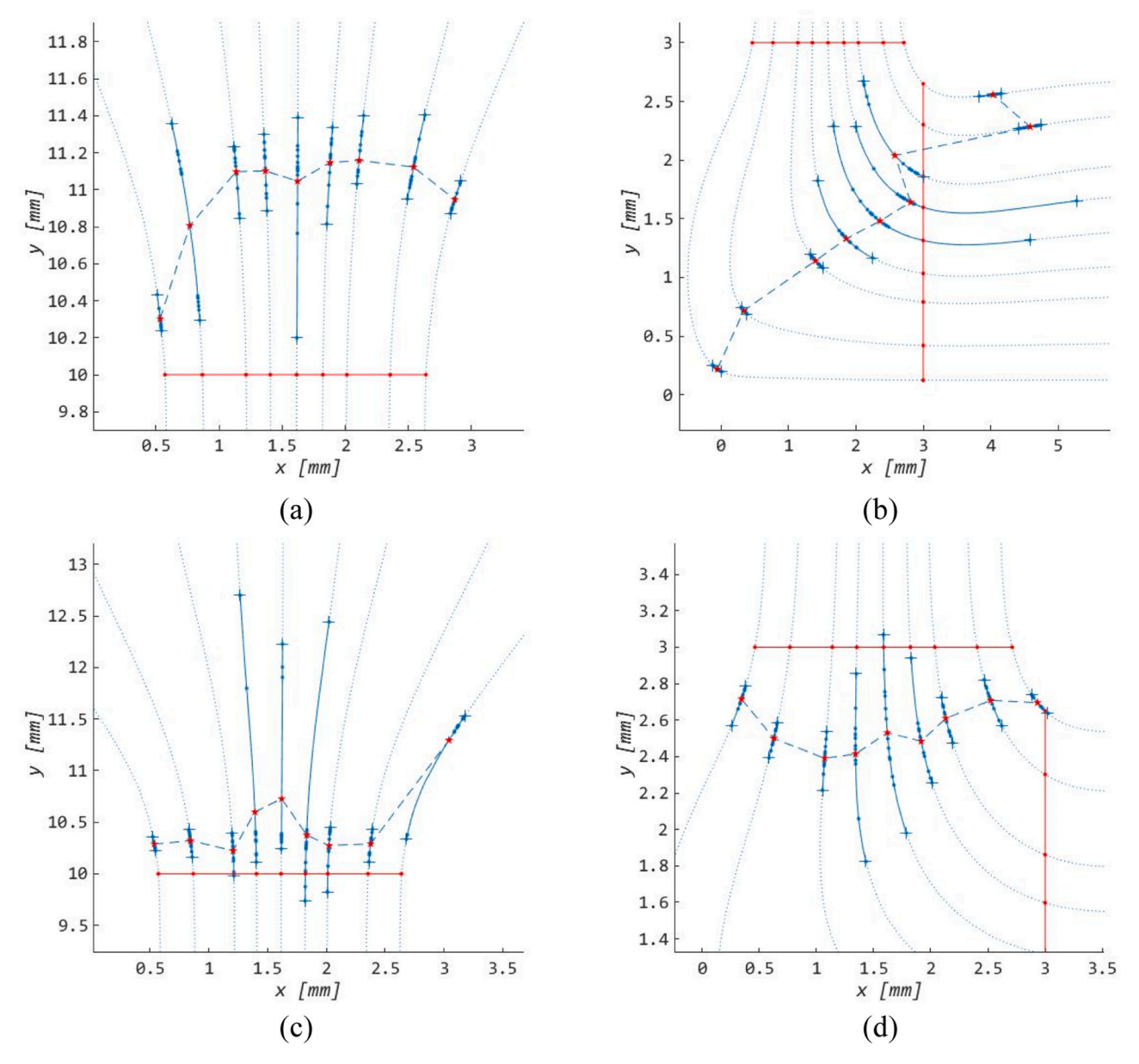


Fig. 19. Distribution of location within the nozzle where the pressure extremes on the fiber surface occurs over the complete period of deposition and for all computed streamlines: (a) overall minimum at Loc. 1 (b) overall minimum at Loc. 2 (c) overall maximum at Loc. 1 (d) overall maximum at Loc. 2.

average extreme maximum pressure at the first peak location (Loc. 1) across streamlines of the nozzle just before zone 1 is seen to be generally less severe than pressure values at the second peak location (Loc. 2), and the mean extreme pressure magnitudes decline asymmetrically with a trough-like appearance from streamlines closer to the edges towards the centerline (cf. Fig. 18c). The opposite behavior is observed at the second extreme site (Loc. 2) where there is an unsymmetrical rise in the mean extreme pressure magnitude from the edges to the centerline in a crest-like manner (cf. Fig. 18d), and the spatial position where this occurs is seen just after the nozzle exit, about .5 mm beneath zone 2 almost nearly evenly across the flow (cf. Fig. 19d). This behavior may be attributed to the relatively high shear rates at the wall just before exiting the nozzle compared to the center streamline which transitions abruptly at the edges.

The result of the fiber's orientation distribution relative to the streamline direction at the 3 regions of interest shows that the fiber is almost nearly aligned with the streamlines of the flow across the nozzle section and the degree of alignment increases towards the edge of the

nozzle as we observe from Fig. 20(a-c). This is consistent with the conclusion of Saffman [51] who observed that the fibers tend to align with the flow. The error bounds of the fiber's orientation across the nozzle due to the variation of initial fiber angle in all three locations are also similar.

4. Conclusion

A computational multiscale FEA methodology has been developed to study the behavior of suspended rigid ellipsoidal fibers during polymer composite melt extrusion-deposition flow through a LAAM nozzle. Sensitivity analysis based on Jeffery's model assumption reveals a direct correlation between the extreme pressures on the fiber surface with its geometry aspect ratio and the rheological properties of the flow (shear rate and viscosity) and these pressure extremes are observed to occur at the fiber's tips. Further, extreme minimum pressures are shown to occur at the fiber tips as the fiber rotates to become more aligned with the flow. Results of the extrusion-deposition multi-scale analysis that

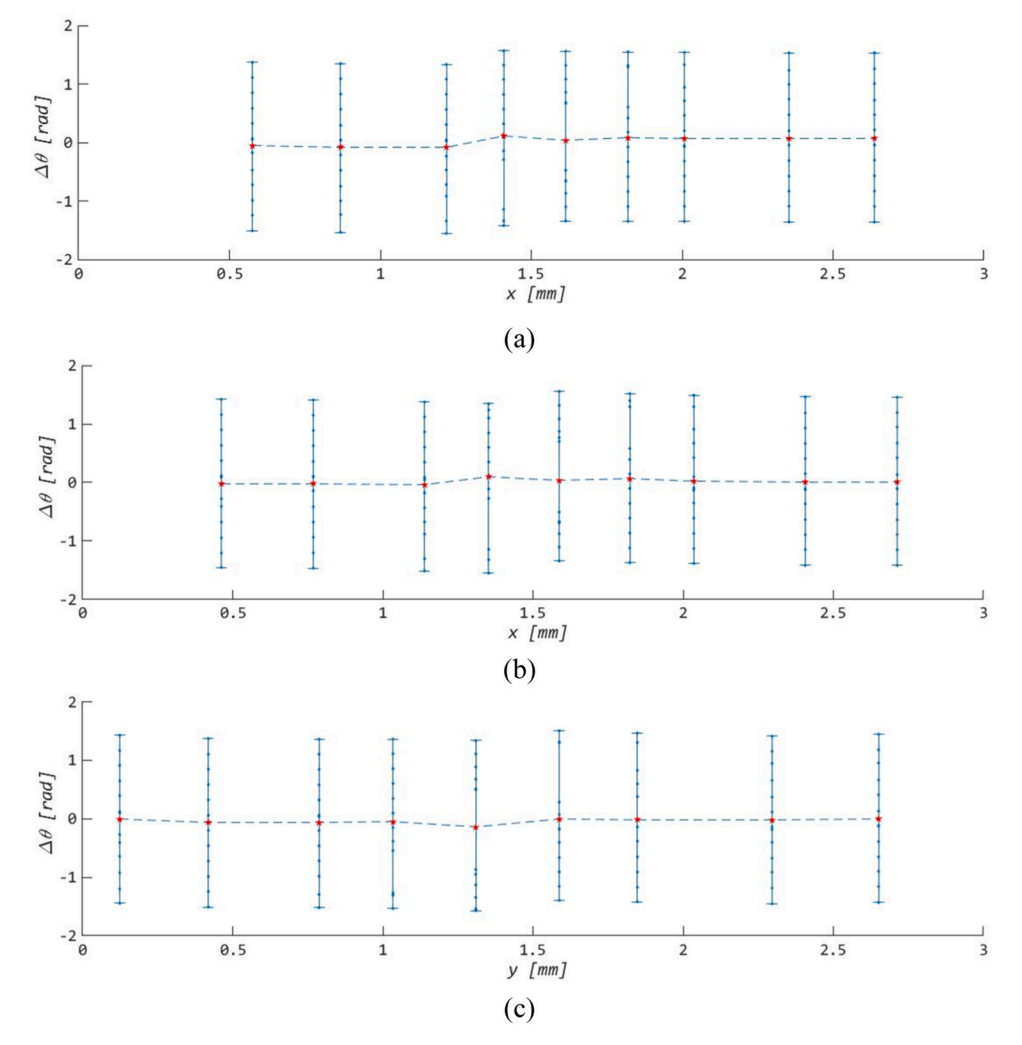


Fig. 20. Distribution of fiber orientation angle at the region of interest within the extruder nozzle: (a) Zone 1 (b) Zone 2 (c) Zone 3.

considers the effect of rotary diffusion due to short-range fiber interaction reveals a dependence of the severity and sensitivity of the fibers extreme pressures to streamline location and the initial fiber orientation. In addition, the effect of increasing fiber concentration and aspect ratio increases the magnitude of the pressure extremes on the fiber surface. In the extrusion-deposition flow, a significant minimum pressure extreme occurs on the fiber surface which at the entrance to the straight capillary section and across the die swell region immediately outside of the extruder nozzle which indicates an increased likelihood for micro-voids initiation at fiber ends in these regions. Results indicate that we would expect a higher probability of occurrence of micro-voids closer to the plate than the free surface. Results also confirm a high degree of the fiber alignment in the extruded bead.

CRediT authorship contribution statement

Smith Douglas E: Writing – review & editing, Validation, Supervision, Software, Resources, Project administration, Methodology, Investigation, Funding acquisition, Conceptualization. **Awenlimobor Aigbe** E: Writing – review & editing, Writing – original draft, Visualization,

Validation, Methodology, Investigation, Formal analysis, Data curation. Wang Zhaogui: Formal analysis.

Declaration of Competing Interest

The authors declare the following financial interests/personal relationships which may be considered as potential competing interests: Douglas Smith reports financial support was provided by National Science Foundation. If there are other authors, they declare that they have no known competing financial interests or personal relationships that could have appeared to influence the work reported in this paper.

Data availability

Data will be made available on request.

Acknowledgement

The authors would like to acknowledge the financial support for this research by National Science Foundation grant #2055628.

Appendix I. - Void Formation Hypothesis

The computational approach presented above predicts the pressure distribution on individual fibers and considers this as a means to assess the likelihood of void formation within the composite melt. The motivation for evaluating pressure on the fiber surface stems from classical nucleation

theory that addresses void initiation and growth within a polymer melt investigated by Han and Han [12], Stewart [13], and Han [14], who also investigated the dynamics of void initiation in polymer melts under shear flow. Colton and Suh [15] distinguished between two mechanisms of nucleation which includes 1) homogenous classification involving the formation of a new stable phase in a primary phase with dissolved secondary components under critical conditions due to thermal fluctuations and molecular interaction and 2) a heterogenous classification involving the crystallization of a third phase at the interface of two other phases, usually a liquid and a solid. Both forms of nucleation can coexist and occur concurrently under a mixed classification. However, in a system such as a colloidal solution, depending on the volume fraction of the suspension, a heterogenous nucleation is more likely to be dominant due to smaller activation energy barrier. The polymer melt material considered in the simulations above is composed of 13% filled carbon fiber ABS (Acrylonitrile Butadiene Styrene) such that a heterogenous dominant mode of nucleation is expected to occur at the interface of the carbon fiber and polymer. Also, it is expected that the polymer material has some degree of absorbed moisture or dissolved additives/volatile.

In the model development by Roychowdhury et. al. [11], a necessary requirement for potential homogenous void nucleation is the occurrence of very low localized fluid pressure P_L below the moisture vapor pressure P_V i.e., $P_L < P_V$ at process temperature Θ_p . The nucleation rate J_n (i.e., $J_n \ge 1$ for void nucleation) as modified by Colton and Suh [15] in heterogenous systems is:

$$J_n = N_v \sqrt{\frac{2\eta}{\pi m}} \exp\left[-\frac{16\pi\eta^3}{3k_B \Theta(P_V - P_L)^2} S(\varphi)\right]$$
(36)

where N_v is the number of molecules per unit volume of the volatile phase, m is the molecular mass of the volatile phase, η is the surface tension at characteristics temperature Θ , and k_B is the Boltzmann constant. In the above,

$$S(\varphi) = (1/4)(2 + \cos\varphi)(1 - \cos\varphi)^2 \tag{37}$$

where φ is the wetting angle of the interface. Usually, the characteristics temperature of nucleation Θ_n stays well above the glass transition/melt temperature Θ_g/Θ_m (i.e., $\Theta_n \sim \Theta_p \geq \Theta_g/\Theta_m$) and the phenomenon takes place almost instantaneously. Colton and Suh [15] determined the moisture vapor pressure from the moisture concentration distribution in the polymer using Henry's Law, $P_V = c/H_V$ where c is the concentration and H_V is Henry's constant for moisture in a polymer. Based on classical nucleation theory, the characteristics nucleation time t_n is given by:

$$t_n = r_c^2/D \tag{38}$$

where D is the moisture diffusivity defined by $D = D_0 e^{-A_E/\Theta}$; and D_0 is the moisture diffusion constant within the polymer, A_E is an activation energy related material constant, and Θ is the temperature. r_c is the critical radius on nucleation given by:

$$r_c = 2\eta/(P_V - P_L) \tag{39}$$

The single fiber pressure solutions appearing above show that the calculated localized fluid pressure P_L (i.e., the minimum pressure extremes calculated in the micro-model) may fall below processing pressure P_W which increases propensity for void nucleation at these sites.

An additional requirement for void nucleation is that the void nucleation time t_n must be less than the streamline deposition time t_d . i.e., $t_n < t_d$. Han and Han [12] showed that the classical nucleation theory under predicts the propensity for void nucleation in polymer solutions with significant proportion of dissolved volatile components. They observed nucleation at critical pressures P_L above the vapor pressure P_V and developed a more applicable model incorporating the Flory Huggins theorem to account for reduced entropies due to restrictions posed by macromolecules in the solvent yielding a nucleation rate of:

$$J_n = [N_v][B_F]e^{\left(-\Delta F_p^*/nk_B\Theta\right)} \tag{40}$$

where B_F is the frequency factor given by:

$$B_F = B_1 \left[D(\Theta) / 4\pi r_{\perp}^2 \right] \exp(-B_2 / \Theta) \tag{41}$$

and $D(\Theta)$ is the molecular diffusivity of the volatile phase which Han and Han [12] obtained using free volume theory of Vrentas and Duda given by:

$$D(\Theta) = D_o(1 - 2\chi_F \theta_1)(1 - \theta_1)^2 \exp(-E/R_G\Theta) \exp(\varsigma(w_1 \widehat{V}_1^* + w_2 \widehat{V}_{\gamma Q}^*)/\widehat{V}_{HF}^*)$$
(42)

The free energy for critical void nucleation in polymer solutions ΔF_p^* given by:

$$\Delta F_{p}^{*} = (16/3)\pi\eta^{3}(P_{V} - P_{L})^{2} - nk_{B}\Theta\left\{\ln\left(\theta_{1}\frac{P_{G}}{P_{V}}\right) + \theta_{2}\left(1 - \frac{V_{1}}{V_{2}}\right) + \chi_{F}\theta_{2}^{2}\right\}$$
(43)

In Eqs. 41 through 43, B_1 & B_2 are empirical constants dependent on the polymer solution, w_i , ϑ_i and V_i are the weight fraction, volume fraction and molar volume of constituent i respectively, subscript i=1 for solvent and i=2 for solute. In our material systems, the proportion of molar volume of the volatile phase in the polymer is much less than unity, i.e., $V_1/V_2\ll 1$, ς is the free volume overlap factor, q is the critical molar volume ratio of jumping units of solvent to jumping units of polymer solution, and \widehat{V}_{HF}^* is the average hole free volume per gram of mixture. χ_F is the Flory Huggins interaction parameter and P_G/P_V defines the degree of saturation of the gas phase, P_G being the pressure inside the critical bubble given as:

$$P_G = (3/2)\rho_L \dot{r}_c^2 + 2\eta/r_c + 4\mu_0 (\dot{r}_c/r_c) + P_L \tag{44}$$

were \dot{r}_c is the growth rate at the onset of nucleation, ρ_L is the liquid density and μ_0 is the viscosity at zero shear.

The surface tension η at the elevated temperature at which the polymers are processed is estimated using expression by Sugden [55] thus:

$$\eta(\Theta) = (P_{\sigma}/\overline{V}(\Theta))^4$$
 (45)

where P_a is the Parachor and $\overline{V}(\Theta)$ is the molar volume of the liquid. The consequence of this is that the surface tension at an elevated temperature can be estimated with knowledge of the surface tension at a reference temperature through:

$$\eta(\Theta_2) = \eta(\Theta_1) \left[\frac{\rho(\Theta_2)}{\rho(\Theta_1)} \right]^4 \tag{46}$$

and the contact angle can be obtained from equation by Girifalco and Good [55].

$$\cos\varphi = 2\widehat{\varphi}\sqrt{(\eta_s/\eta_l)} - 1, \ \widehat{\varphi} = 4\left[V_s^{-1/3} + V_l^{-1/3}\right]^{-1}, \ V = \frac{N_v}{\rho}$$
(47)

The details here provide a possible basis for estimating the potential for void nucleation within a polymer melt given a known amount of volatile content in future research.

Appendix II. - Two-Dimensional (2D) Reduced Form of Jeffery's Equation

The 2D contracted form of the Jeffery's pressure and velocity [32] can be expressed by Eqs. (48) and (49) respectively given as:

$$p = p_0 + 2\mu \left\{ A \frac{\partial^2 \Omega}{\partial^2 x} + B \frac{\partial^2 \Omega}{\partial^2 y} + (H + H') \frac{\partial^2 \Omega}{\partial x \partial y} \right\}$$
 (48)

$$\begin{bmatrix} v_{x} \\ v_{y} \end{bmatrix} = \begin{bmatrix} v_{x}^{0} \\ v_{y}^{0} \end{bmatrix} + \begin{bmatrix} Y & W \\ -W & Y \end{bmatrix} \begin{bmatrix} \frac{\partial \chi_{3}}{\partial x} \\ \frac{\partial \chi_{3}}{\partial y} \end{bmatrix} + \begin{bmatrix} \frac{\partial^{2} \Omega}{\partial x^{2}} & \frac{\partial^{2} \Omega}{\partial x \partial y} \\ \frac{\partial^{2} \Omega}{\partial x \partial y} & \frac{\partial^{2} \Omega}{\partial y^{2}} \end{bmatrix} \begin{bmatrix} A & H \\ H' & B \end{bmatrix}^{T} \begin{bmatrix} x \\ y \end{bmatrix} - \begin{bmatrix} A & H \\ H' & B \end{bmatrix} \begin{bmatrix} \frac{\partial \Omega}{\partial x} \\ \frac{\partial \Omega}{\partial y} \end{bmatrix}$$

$$(49)$$

Alternatively, this can be written as:

$$p = p_0 + 2\mu \underline{Z}_{\underline{v}} : \underline{\nabla}_{\underline{v}}^2 \Omega \tag{50}$$

$$\underline{v} = \underline{v}_0 + \underline{\underline{Z}}_{\chi} \bullet \underline{\nabla}_{\chi} \chi_3 + \underline{\underline{\nabla}}_{\chi}^2 \Omega \quad \bullet \left[\underline{\underline{Z}}_{\chi}^T \bullet \underline{X} \right] - \underline{\underline{Z}}_{\chi} \bullet \underline{\nabla}_{\chi} \Omega$$
(51)

Where p_0 is the constant mean pressure at a distance from the ellipsoid, $\underline{v} = \begin{bmatrix} v_x & v_y \end{bmatrix}^T$ are the velocity components at arbitrary position (x,y) and $\underline{v}_0 = \begin{bmatrix} v_x^0 & v_y^0 \end{bmatrix}^T$ is the velocity of the undisturbed fluid at (x,y) given as:

$$v_0 = \nabla v \bullet X \tag{52}$$

coefficient matrices $\underline{\underline{Z}}_{x}$ and $\underline{\underline{Z}}_{x}$ and the gradient and hessian operators $\underline{\nabla}_{x}$ and $\underline{\nabla}_{x}^{2}$ are respectively given as:

$$\underline{\underline{Z}}_{\chi} = \begin{bmatrix} Y & W \\ -W & Y \end{bmatrix}, \ \underline{\underline{Z}}_{\chi} = \begin{bmatrix} A & H \\ H' & B \end{bmatrix}, \ \underline{\underline{\nabla}}_{\chi} = \begin{bmatrix} \frac{\partial}{\partial x} \\ \frac{\partial}{\partial y} \end{bmatrix}, \ \underline{\underline{\nabla}}_{\chi}^{2} = \begin{bmatrix} \frac{\partial^{2}}{\partial x^{2}} & \frac{\partial^{2}}{\partial x \partial y} \\ \frac{d^{2}}{\partial y \partial x} & \frac{\partial^{2}}{\partial y^{2}} \end{bmatrix}$$

The 2D strain deformation tensor in the local fiber reference frame $\underline{\nabla v}$ is decomposed in the usual way to obtain the 2D symmetric component $\underline{\underline{\Gamma}}$ and anti-symmetric components $\underline{\omega}$ according to:

$$\underline{\nabla v} = \underline{\Gamma} + \underline{\omega} \tag{53}$$

$$\underline{\underline{\Gamma}} = \underline{\nabla v} + \underline{\nabla v}^T = \begin{bmatrix} \varepsilon & h \\ h & -\varepsilon \end{bmatrix}, \ \underline{\underline{\omega}} = \omega \underline{\underline{G}} = \underline{\nabla v} - \underline{\nabla v}^T, \ \underline{\underline{G}} = \begin{bmatrix} & -1 \\ 1 & \end{bmatrix}$$
 (54)

The 2D Laplace Function Ω that appears in Eqs. (48) - (51) is defined as:

$$\Omega = \int_{\zeta}^{\infty} \frac{1}{\Delta} \left\{ \frac{x^2}{a^2 + \zeta} + \frac{y^2}{b^2 + \zeta} - 1 \right\} d\zeta \tag{55}$$

where

$$\Delta = \left\{ \left(a^2 + \zeta \right) \left(b^2 + \zeta \right) \right\}^{1/2}, \ and, \ \zeta : \frac{x^2}{a^2 + \zeta} + \frac{y^2}{b^2 + \zeta} = 1$$
 (56)

At the fiber's surface where $\zeta = 0$, the field velocity must equal the fiber's surface velocity assuming no slip at the fiber's surface, i.e.

$$\underline{\underline{v}}\Big|_{\underline{c}=0} = \dot{\theta}\underline{\underline{G}} \bullet \underline{\underline{X}} \tag{57}$$

The constants that appear in $\underline{\underline{Z}}_{v}$, $\underline{\underline{Z}}_{x}$ above are thus obtained as:

$$A = -B = \frac{\varepsilon}{4\gamma_0'}, \ H = H' = \frac{1}{2} \left[\frac{\omega - \dot{\theta}}{\alpha_0 - \beta_0} \right], \ Y = -\frac{h}{\gamma_0'}, \ W = 2(a^2 + b^2)A$$
 (58)

where $\alpha_0, \beta_0, \gamma_0, \gamma_0' \alpha \chi_3$ retain their usual definition given [32]. The fibers angular velocity is derived as:

$$\dot{\theta} = \omega + \frac{(a^2 - b^2)}{(a^2 + b^2)} h \tag{59}$$

References

- [1] K. Rajaguru, T. Karthikeyan, V. Vijayan, Additive manufacturing-state of art, Mater. Today Proc. 21 (2020) 628–633.
- [2] M. Mehdikhani, L. Gorbatikh, I. Verpoest, S.V. Lomov, Voids in fiber-reinforced polymer composites: a review on their formation, characteristics, and effects on mechanical performance, J. Compos. Mater. 53 (12) (2019) 1579–1669.
- [3] N. Van de Werken, H. Tekinalp, P. Khanbolouki, S. Ozcan, A. Williams, M. Tehrani, Additively manufactured carbon fiber-reinforced composites: state of the art and perspective, Addit. Manuf. 31 (2020) 100962.
- [4] J.J. Fallon, S.H. McKnight, M.J. Bortner, Highly loaded fiber filled polymers for material extrusion: a review of current understanding, Addit. Manuf. 30 (2019) 100810
- [5] H.L. Tekinalp, V. Kunc, G.M. Velez-Garcia, C.E. Duty, L.J. Love, A.K. Naskar, C. A. Blue, S. Ozcan, Highly oriented carbon fiber–polymer composites via additive manufacturing, Compos. Sci. Technol. 105 (2014) 144–150. Dec 10.
- [6] A. Vaxman, M. Narkis, A. Siegmann, S. Kenig, Void formation in short-fiber thermoplastic composites, Polym. Compos. 10 (6) (1989) 449–453.
- [7] E.A. Papon, A. Haque, Review on process model, structure-property relationship of composites and future needs in fused filament fabrication, J. Reinf. Plast. Compos. 39 (19-20) (2020) 758–789.
- [8] S. Yu, H. Bale, S. Park, J.Y. Hwang, S.H. Hong, Anisotropic microstructure dependent mechanical behavior of 3D-printed basalt fiber-reinforced thermoplastic composites, Compos. Part B Eng. 224 (2021) 109184.
- [9] N. Sayah, D.E. Smith, Effect of process parameters on void distribution, volume fraction, and sphericity within the bead microstructure of large-area additive manufacturing polymer composites, Polymers 14 (23) (2022) 5107.
- [10] M. Narkis, A. Vaxman, S. Kenig, A. Siegmann, Quantitative measurement of fiber orientation and fracture, void and weld-lines in short fiber reinforced thermoplastic composites, J. Thermoplast. Compos. Mater. 2 (4) (1989) 307–318.
- [11] S. Roychowdhury, J.W. Gillespie Jr, S.G. Advani, Volatile-induced void formation in amorphous thermoplastic polymeric materials: I. Modeling and parametric studies, J. Compos. Mater. 35 (4) (2001) 340–366.
- [12] J.H. Han, C. Dae Han, Bubble nucleation in polymeric liquids. II. Theoretical considerations, J. Polym. Sci. Part B Polym. Phys. 28 (5) (1990) 743–761.
- [13] C.W. Stewart, Nucleation and growth of bubbles in elastomers, J. Polym. Sci. Part A-2 Polym. Phys. 8 (6) (1970) 937–955.
- [14] Han, J.H.P., 1988. Bubble Nucleation in Polymeric Liquids (Doctoral dissertation), Polytechnic Institute of NewYork.
- [15] J.S. Colton, N. Suh, The nucleation of microcellular thermoplastic foam with additives: Part I: theoretical considerations, Polym. Eng. Sci. 27 (7) (1987) 485–492.
- [16] G. Titomanlio, S. Piccarolo, G. Marrucci, Analysis of void formation in extruded bars, Polym. Eng. Sci. 25 (2) (1985) 91–97.
- [17] G. Titomanlio, S. Piccarolo, G. Marrucci, Non-Newtonian analysis of void formation in extruded polymeric bars, Chem. Eng. Commun. 53 (1-6) (1987) 49–59.
- [18] Y. Eom, L. Boogh, V. Michaud, P. Sunderland, J.A. Månson, Stress-initiated void formation during cure of a three-dimensionally constrained thermoset resin, Polym. Eng. Sci. 41 (3) (2001) 492–503 (Mar).
- [19] D. Yang, H. Zhang, J. Wu, E.D. McCarthy, Fibre flow and void formation in 3D printing of short-fibre reinforced thermoplastic composites: an experimental benchmark exercise, Addit. Manuf. 37 (2021) 101686.
- [20] H. Xia, J. Lu, S. Dabiri, G. Tryggvason, Fully resolved numerical simulations of fused deposition modeling. Part I: fluid flow, Rapid Prototyp. J. 24 (2) (2018)
- [21] B.P. Heller, D.E. Smith, D.A. Jack, Planar deposition flow modeling of fiber filled composites in large area additive manufacturing, Addit. Manuf. 25 (2019)
- [22] Wang, Z., 2019. Computational Modeling of Fiber Reinforced Composites Melt Flow in Nozzle Extrudate for Polymer Deposition Additive Manufacturing (Doctoral dissertation), Baylor University.
- [23] Z. Wang, D.E. Smith, A fully coupled simulation of planar deposition flow and fiber orientation in polymer composites additive manufacturing, Materials 14 (10) (2021) 2596.

- [24] Wang, Z., Luo, C., Xie, Z., Fang, Z., Three-dimensional polymer composite flow simulation and associated fiber orientation prediction for large area extrusion deposition additive manufacturing, Polym. Compos., 44 (10), 6720–6735.
- [25] T. Russell, B. Heller, D.A. Jack, D.E. Smith, Prediction of the fiber orientation state and the resulting structural and thermal properties of fiber reinforced additive manufactured composites fabricated using the big area additive manufacturing process. J. Compos. Sci. 2 (2) (2018) 26.
- [26] D.D. Phan, J.S. Horner, Z.R. Swain, A.N. Beris, M.E. Mackay, Computational fluid dynamics simulation of the melting process in the fused filament fabrication additive manufacturing technique, Addit. Manuf. 33 (2020) 101161.
- [27] N. Shadvar, E. Foroozmehr, M. Badrossamay, I. Amouhadi, A.S. Dindarloo, Computational analysis of the extrusion process of fused deposition modeling of acrylonitrile-butadiene-styrene, Int. J. Mater. Form. 14 (1) (2021) 121–131.
- [28] D. Yang, K. Wu, L. Wan, Y. Sheng, A particle element approach for modelling the 3D printing process of fibre reinforced polymer composites, J. Manuf. Mater. Process. 1 (1) (2017) 10.
- [29] Z. Ouyang, E. Bertevas, L. Parc, et al., A smoothed particle hydrodynamics simulation of fiber-filled composites in a non-isothermal three-dimensional printing process, Phys. Fluids 31 (12) (2019) 123102.
- [30] Oberbeck, A., 1876. Ueber stationäre Flüssigkeitsbewegungen mit Berücksichtigung der inneren Reibung, 62–80.
- [31] D. Edwardes, Steady motion of a viscous liquid in which an ellipsoid is constrained to rotate about a principal axis, Quart. J. Math. 26 (70-78) (1892) 68.
- [32] G.B. Jeffery, The motion of ellipsoidal particles immersed in a viscous fluid, Proc. R. Soc. Lond. Ser. A 102 (715) (1922) 161–179.
- [33] E.J. Hinch, L.G. Leal, Rotation of small non-axisymmetric particles in a simple shear flow, J. Fluid Mech. 92 (3) (1979) 591–607.
- [34] D. Zhang, D. E Smith, D. A Jack, S. Montgomery-Smith, Numerical evaluation of single fiber motion for short-fiber-reinforced composite materials processing, J. Manuf. Sci. Eng. 133 (5) (2011).
- [35] J. Férec, G. Ausias, G. Natale, May. Numerical evaluation of a single ellipsoid motion in Newtonian and power-law fluids, in: AIP Conference Proceedings, 1960, AIP Publishing LLC, 2018 020006.
- [36] S.A. Abtahi, G.J. Elfring, Jeffery orbits in shear-thinning fluids, Phys. Fluids 31 (10) (2019) 103106.
- [37] P. Skjetne, R.F. Ross, D.J. Klingenberg, Simulation of single fiber dynamics, J. Chem. Phys. 107 (6) (1997) 2108–2121.
- [38] S. Yamamoto, T. Matsuoka, A method for dynamic simulation of rigid and flexible fibers in a flow field, J. Chem. Phys. 98 (1) (1993) 644–650.
- [39] M. Yamanoi, J.M. Maia, Stokesian dynamics simulation of the role of hydrodynamic interactions on the behavior of a single particle suspending in a Newtonian fluid. Part 1. 1D flexible and rigid fibers, J. Non Newton. Fluid Mech. 166 (9-10) (2011) 457–468.
- [40] S.K. Kugler, A. Kech, C. Cruz, T. Osswald, Fiber orientation predictions—a review of existing models, J. Compos. Sci. 4 (2) (2020) 69.
- [41] Zhang, D., 2013. Flow-Induced Micro-and Nano-Fiber Suspensions in Short-Fiber Reinforced Composite Materials Processing (Doctoral dissertation) University of Missouri-Columbia.
- [42] D. Zhang, D.E. Smith, Finite element-based brownian dynamics simulation of nanofiber suspensions using Monte Carlo Method, J. Micro Nano Manuf. 3 (4) (2015).
- [43] D. Zhang, D.E. Smith, Dynamic simulation of discrete fiber motion in fiber-reinforced composite materials processing, J. Compos. Mater. 50 (10) (2016) 1301–1319.
- [44] Z. Wang, D.E. Smith, A fully coupled simulation of planar deposition flow and fiber orientation in polymer composites additive manufacturing, Materials 14 (10) (2021) 2506
- [45] Reddy, J.N., 2019. Introduction to the Finite Element Method, McGraw-Hill Education.
- [46] J.N. Reddy, D.K. Gartling, The Finite Element Method in Heat Transfer and Fluid Dynamics, CRC Press, 2010.
- [47] Carlsson, A., 2007. Orientation of Fibres in Suspensions Flowing over A Solid Surface (Doctoral dissertation), KTH.
- [48] A. Awenlimobor, Z. Wang, D.E. Smith, Physical modeling: simulation of micro-void development within large scale polymer composite deposition beads. in:

- Proceedings of the 2021 International Solid Freeform Fabrication Symposium, University of Texas at Austin, 2021.
- [49] F. Folgar, C.L. Tucker III, Orientation behavior of fibers in concentrated suspensions, J. Reinf. Plast. Compos. 3 (2) (1984) 98–119.
- [50] S.G. Advani, C.L. Tucker III, The use of tensors to describe and predict fiber orientation in short fiber composites, J. Rheol. 31 (8) (1987) 751–784.
- [51] P.G. Saffman, On the motion of small spheroidal particles in a viscous liquid, J. Fluid Mech. 1 (5) (1956) 540–553.
- [52] VerWeyst, B.E., 1998. Numerical Predictions of Flow-induced Fiber Orientation in Three-dimensional Geometries (Doctoral dissertation), University of Illinois at Urbana-Champaign.
- [53] Awenlimobor A., Smith D.E., 2023. Determination of Preferred Fiber Orientation State based on Newton – Raphson Method using on Exact Jacobian. Baylor University, Waco, TX. Unpublished.
- [54] Bay, R.S., 1991. Fiber Orientation in Injection-molded Composites: a Comparison of Theory and Experiment (Doctoral dissertation) University of Illinois at Urbana-Champaign.
- [55] A. Agrawal, Surface tension of polymers. Hatsopoulos Microfluids Laboratory, Department of Mechanical Engineering, Massachusetts Institute of Technology, 2005.